The Astrophysical Journal, 846:51 (27pp), 2017 September 1 https://doi.org/10.3847/1538-4357/aa855f

X-Ray Morphological Analysis of the Planck ESZ Clusters

Lorenzo Lovisari[1], William R. Forman[1], Christine Jones[1], Stefano Ettori[2,3], Felipe Andrade-Santos[1], Monique Arnaud[4], Jessica Démoclès[4], Gabriel W. Pratt[4], Scott Randall[1], and Ralph Kraft[1]
[1] Harvard-Smithsonian Center for Astrophysics, 60 Garden Street, Cambridge, MA 02138, USA
[2] INAF, Osservatorio Astronomico di Bologna, via Ranzani 1, I-40127 Bologna, Italy
[3] INFN, Sezione di Bologna, viale Berti Pichat 6/2, I-40127 Bologna, Italy
[4] Laboratoire AIM, IRFU/Service d'Astrophysique—CEA/DRF—CNRS—Université Paris Diderot, Bât. 709, CEA-Saclay, F-91191 Gif-sur-Yvette Cedex, France
Received 2017 May 3; revised 2017 August 1; accepted 2017 August 7; published 2017 August 31

Abstract

X-ray observations show that galaxy clusters have a very large range of morphologies. The most disturbed systems, which are good to study how clusters form and grow and to test physical models, may potentially complicate cosmological studies because the cluster mass determination becomes more challenging. Thus, we need to understand the cluster properties of our samples to reduce possible biases. This is complicated by the fact that different experiments may detect different cluster populations. For example, Sunyaev–Zeldovich (SZ) selected cluster samples have been found to include a greater fraction of disturbed systems than X-ray selected samples. In this paper we determine eight morphological parameters for the Planck Early Sunyaev–Zeldovich (ESZ) objects observed with *XMM-Newton*. We found that two parameters, concentration and centroid shift, are the best to distinguish between relaxed and disturbed systems. For each parameter we provide the values that allow selecting the most relaxed or most disturbed objects from a sample. We found that there is no mass dependence on the cluster dynamical state. By comparing our results with what was obtained with REXCESS clusters, we also confirm that the ESZ clusters indeed tend to be more disturbed, as found by previous studies.

Key words: galaxies: clusters: intracluster medium – X-rays: galaxies: clusters

1. Introduction

Galaxy clusters were first detected as high concentrations of galaxies in the sky. In addition to the galaxies, there is a hot X-ray emitting intracluster medium (ICM) that accounts for the bulk of the cluster baryons. That makes X-ray surveys a powerful tool for cluster detection. More recently, Sunyaev–Zeldovich (SZ, Sunyaev & Zeldovich 1972) observations have opened a new window for cluster detection and are now providing new catalogs. Owing to the different dependence of the SZ and X-ray emission on the gas density, there is currently a debate regarding whether the two experiments are detecting the same population of galaxy clusters. In particular, since the X-ray emission scales with the square of the gas density, X-ray surveys are more prone to detect centrally peaked, more relaxed galaxy clusters (e.g., Eckert et al. 2011). Being less sensitive to the central gas density, the SZ experiments detect more unrelaxed clusters (e.g., Planck Collaboration et al. 2011a).

The first indications that dynamically disturbed objects are more represented in the SZ than X-ray surveys were found by Planck Collaboration et al. (2011a) and Planck Collaboration et al. (2013) by comparing the scaled density profiles of the newly detected SZ clusters with those of REXCESS clusters, a representative X-ray sample. The SZ objects have on average flatter gas density distributions (i.e., have a more disturbed morphology). Recently, Rossetti et al. (2016) used the projected distance between the X-ray peak and the brightest galaxy cluster (BCG) as an indicator of relaxation for galaxy clusters. They found that X-ray selected samples tend to be more relaxed than SZ selected clusters, and they interpreted the result as an indication of the cool-core bias. In a second paper, Rossetti et al. (2017) also investigated another morphological parameter (concentration), and they confirmed their first paper's result and supported the cool-core bias interpretation by performing a set of simulations. The result has also been confirmed by Andrade-Santos et al. (2017), who compared the concentration, cuspiness, and central density for the ESZ sample (only clusters with redshifts lower than 0.35) and an X-ray flux limited sample. Although both papers obtained similar results, they provide a different explanation for the selection effects. Andrade-Santos et al. (2017) described a simple model that predicts that cool-core clusters are over-represented in X-ray samples because of the Malmquist bias, and the authors were able to reproduce their results considering only the average luminosity difference between cool-core and non-cool-core clusters. Rossetti et al. (2017) performed a set of dedicated simulations by considering the different shapes of the surface brightness profile for cool-core and non-cool-core clusters to produce a realistic population of galaxy clusters, and they investigated the effect of the X-ray and SZ selection. They found that Malmquist and cool-core biases are probably at the origin of the different fraction of relaxed systems in the two samples but it probably cannot explain the whole difference. The above-mentioned papers are based on Planck-selected samples, while interestingly, Nurgaliev et al. (2017) did not find significant differences in the observed morphology of X-ray and SPT selected samples using two other methods (i.e., centroid shifts and photon asymmetry). On the other hand, the different papers also used different X-ray samples (with different redshift and mass properties, as well as selection methods) for the comparison, which complicates the interpretation of the different results, as discussed in more detail by Rossetti et al. (2017).

The different fractions of relaxed and unrelaxed systems in the samples have important implications for cosmology. In fact, the cluster mass, which is the most fundamental property of clusters when they are used in cosmological studies, can be over- or underestimated during a cluster merger when clusters are generally not in hydrostatic equlibrium (e.g., Randall et al.

2002). Moreover, compression and heating can alter both temperature and luminosity (e.g., Ricker & Sarazin 2001). Even for relaxed systems, accurate determination of the mass requires good knowledge of both the gas density and temperature profiles up to R_{500},[5] but these parameters are not available for many systems. Moreover, in the future, almost all groups and clusters detected with eROSITA will have too few photons to measure their temperature and mass profiles (Borm et al. 2014). Thus, cosmological studies using groups and clusters of galaxies rely heavily on a detailed understanding of the scaling relations. Measures of the dynamical states of the systems offer important information to obtain precise scaling relations and understand their scatter. For example, Mantz et al. (2015) showed that the identification of substructure in galaxy clusters allowed an accurate selection of relaxed systems that led to tight constraints on the cosmological evolution of the gas mass fraction. Moreover, although we need the mass function of the whole population to test the cosmological models, the X-ray masses, obtained under the assumption of hydrostatic equilibrium, are more robust for relaxed clusters (e.g., Rasia et al. 2006; Lau et al. 2009). A recent study by Applegate et al. (2016), based on relaxed systems, disfavors strong departures from hydrostatic equilibrium and shows a good agreement between X-ray and lensing masses (see also the results by Israel et al. 2014). Andrade-Santos et al. (2012) showed that since disturbed systems tend to be less luminous and less massive, they can be used in the scaling relations when the level of substructures is known and parametrized so that their positions in the mass-observable planes can be corrected (e.g., Ventimiglia et al. 2008). Different from the cosmological studies, astrophysical investigations usually focus more on highly disturbed galaxy clusters where phenomena like turbulence and particle (re-)acceleration are more prominent and easier to be investigated. Furthermore, most of these disturbed galaxy clusters are outliers in many scaling relations, thus their identification is fruitful for many different studies.

Characterizing the dynamical state of a galaxy cluster requires accessing a large set of information in different wavelengths (e.g., gas thermodynamical property distribution from X-ray data and total mass distribution from the lensing analysis), which is available only for a few individual clusters. An alternative is to compute well-defined morphological parameters, making use of the relatively cheap X-ray images and profiles. Several morphological indicators have been proposed in the past few decades: e.g., BCG-X-ray peak offset (e.g., Jones & Forman 1984, 1999), centroid shifts (Mohr et al. 1993), power ratios (Buote & Tsai 1995, 1996), concentration parameter (Santos et al. 2008), and photon asymmetry (Nurgaliev et al. 2013). Pinkney et al. (1996) and Böhringer et al. (2010) showed that because of the different projection effects, none of these methods is good in all cases, and a combination of them might be more effective to quantify the level of substructures. Thus, given the large amount of new data that will be collected from current and future surveys, and because both X-ray and SZ detection methods may have some common biases (Angulo et al. 2012; Lin et al. 2015), it is important to investigate the morphological indicators for large cluster samples and (i) identify which parameter(s) most efficiently allow us to classify relaxed and disturbed objects, and (ii) verify whether the X-ray morphologies of X-ray and SZ samples are consistent.

It is very difficult to subdivide relaxed and disturbed systems because there is no rigorous definition, and a simple subdivision into two classes is probably overly simplistic. In fact, the measure of the level of relaxation of galaxy clusters as given by the morphological parameters is a continuos function, from very relaxed systems (i.e., objects with circular X-ray isophotes and without substructures) to very disturbed objects (i.e., clear evidence of merging). While most of the systems are not on the tail of the distribution, as discussed above, several studies are only interested in the extreme systems (either the most relaxed or the most disturbed). Thus, instead of finding parameter values that split the objects into two subsamples, for these studies, it is more important to have threshold values that selectively exclude most, if not all, the relaxed or unrelaxed systems.

In this paper we study a set of eight morphological parameters. Some of them are derived from the X-ray images, while others are derived from the surface brightness (SB) and electron density profiles. The goal is to identify the best parameters to pinpoint the most relaxed and most disturbed galaxy clusters.

We assume a ΛCDM cosmology with $H_0 = 70\,\mathrm{km\,s^{-1}\,Mpc^{-1}}$, $\Omega_\Lambda = 0.7$ and $\Omega_m = 0.3$. The outline of the paper is as follows. In Section 2 we present the data preparation and analysis. The definitions of the morphological parameters are presented in Section 3 and the results in Section 4. In Sections 5 and 6 we discuss the results and present our conclusions.

2. Data Analysis

2.1. The Sample

Simulations have shown that the SZ quantities weakly depends on the dynamical state of the objects (e.g., Motl et al. 2005), suggesting that SZ selected samples might be more representative of the underlying cluster population and so might be more appropriate for the study we are carrying out in this paper.

ESA's Planck Mission has provided a long list of cluster candidates from which two large and statistically representative samples have been extracted: (i) the ESZ sample (Planck Collaboration et al. 2011b), and (ii) the PSZ1 cosmology sample (Planck Collaboration et al. 2014). Both samples would be suitable for our analyses, but we choose the ESZ sample because when we started this analysis (beginning of 2016), its *XMM-Newton* coverage (public data for 149[6] versus 142 clusters) was larger than the coverage for the PSZ1 cosmological sample.

The ESZ sample consists of 189 massive clusters (one is a false detection), which were selected by imposing a signal-to-noise ratio threshold of 6 on the catalog of Sunyaev–Zel'dovich (SZ) detections above the Galactic plane ($|b| > 15°$). The clusters span a quite broad redshift range, from 0.01 to 0.55. *XMM-Newton* has observed 155 of these Planck clusters, but for 5 of them, the observations are completely flared and cannot be used for the characterization of the cluster properties.

[5] R_{500} corresponds to the radius within which the overdensity of the galaxy cluster is 500 times the critical density of the Universe.

[6] Note that since we started, the data became public for another six clusters, which are also included in the sample.

2.2. Data Reduction

Observation data files (ODFs) were downloaded from the *XMM-Newton* archive and processed with the XMM v.16.0.0 software for data reduction. The initial data processing to generate calibrated event files from raw data was done by running the tasks *emchain* and *epchain*. We only considered single, double, triple, and quadruple events for MOS (i.e., PATTERN $\leqslant$ 12) and single for pn (i.e., PATTERN==0), and we applied the standard procedure for the removal of bright pixels and hot columns (i.e., FLAG==0) and the pn out-of-time correction. All the data were cleaned for periods of high background due to the soft protons, following the procedure extensively described in Lovisari et al. (2015).

2.3. Image Analyses

The X-ray images were created in the 0.3–2 keV energy band to maximize the signal-to-noise ratio using a binning of 82 physical pixels corresponding to a resolution of 4.1 arcsec. The background subtraction was performed using a combination of blank-sky field (BSF) and filter-wheel closed (FWC) observations as described in Lovisari et al. (2011). Briefly, we selected the data sets with the most similar background properties for each cluster. We filtered the events by applying the same selection criteria as were used for the observations. For each detector we added/subtracted the renormalized FWC observations to the corresponding BSF images to compensate for the difference between the out-of-field-of-view (OOFOV) events (which are a good indicator of the level of the particle background) in the observation and in the BSF data. The normalization factors were obtained by fitting the OOFOV events of both the observation and the BSF in the 3–10 keV energy band (for more details about this choice, see Zhang et al. 2009) with a model that includes a power law and several Gaussian lines to account for the fluorescent emission observed in both detectors. The normalization factors were derived as the ratio of the power-law normalization of the observation to the BSF. The data from the three detectors were combined into a single image and divided by the combined exposure map after the MOS exposures were rescaled by a factor to account for the difference in effective area. The weighting factors have been obtained by determining the scaling of the cluster surface brightness profiles observed with each of the three detectors (see Böhringer et al. 2010). Thanks to this procedure, all the gaps (e.g., CCD gaps) are removed from the final images. Regions exposed with less than 5% of the total exposure were excluded.

Point-like X-ray sources were detected with the *edetect-chain* task and visually inspected to discriminate between real point sources and extended cluster substructures. The latter were not removed from the data files. After removing the point sources, the holes were refilled using the CIAO task *dmfilth*.

2.4. Surface Brightness

We determined the surface brightness (SB) profiles, centered on the X-ray peak of the main cluster component, from the background-subtracted, vignetting-corrected images, as described in the previous section. The chosen energy band provides an optimal ratio of the source over background flux for *XMM-Newton* data and ensures an almost temperature-independent X-ray emission. For the calculation of the profiles, to avoid "humps" in the SB profiles due to the presence of substructures or a secondary peak (e.g., in the case of an infalling system), we removed all substructures clearly visible by eye. For bimodal mergers, the profiles were obtained independently for the two subclusters. The SB profiles were fitted with a double β-model:

$$S_X(r) = \sum_{i=1}^{2} S_{0,i}\left[1 + \left(\frac{r}{r_{c,i}}\right)^2\right]^{-3\beta+0.5}, \quad (1)$$

where $r_{c,i}$ and $S_{0,i}$ are the core radius and central surface brightness of each of the two components, respectively. This model usually provides a good fit for all the clusters after the main substructures are removed.

2.5. R_{500}

Galaxy clusters are at the nodes of the cosmic web, which means that at large radii, they are expected to show signatures of accretion processes (e.g., Roncarelli et al. 2006). Hydrodynamical simulations have shown that within R_{500}, galaxy clusters are relatively relaxed unless a merger event modifies the existing conditions. Thus, R_{500} represents the optimal radius for the morphological analysis to obtain a comprehensive view of the dynamical state of the clusters. Because of their low redshifts, a small fraction of objects do extend beyond the *XMM-Newton* field of view (FOV), so we also computed the morphological parameters within $0.5R_{500}$.

Using the spectral temperature, $T_{\rm init}$, measured in the region that maximizes the signal-to-noise ratio in the 0.3–2 keV band, we estimated an initial $R_{500,\rm init}$ using the equation from Arnaud et al. (2005):

$$R_{500,\rm init} = 1.104 \times (T_{\rm init}/5\ {\rm keV})^{0.57} E(z)^{-1}, \quad (2)$$

where $E(z)$ is the ratio of the Hubble constant at redshift z to its present-day value. We then calculated the total gas mass ($M_{\rm gas}$) by integrating the density profile within that radius and computed $Y_X = M_{\rm gas} \times T_{\rm init}$. By using the M-Y_X relation given in Arnaud et al. (2010), assuming self-similar evolution,

$$E(z)^{0.4} M_{500} = 10^{14.567}\left[\frac{Y_{X,500}}{2 \times 10^{14} M_\odot\,{\rm keV}}\right]^{0.561} M_\odot, \quad (3)$$

we estimate M_{500} and R_{500}. We then re-extracted a spectrum in the region within 0.15–$0.75R_{500}$ to determine a new temperature and recomputed Y_X using the new R_{500} and M_{500}. The procedure was repeated until convergence, which occurs when the difference between the initial and the new temperature is smaller than 1%.

The spectral analyses were made using XSPEC (Arnaud 1996). All the spectra were rebinned to ensure at least 25 counts per bin and a minimum energy width per bin of one-third of the FWHM to prevent oversampling the instrument spectral resolution. Spectra were fit in the 0.3–10 keV energy range with an absorbed APEC (Smith et al. 2001) thermal plasma with a column density from Willingale et al. (2013). The EPIC spectra were fitted simultaneously, with temperatures and metallicities linked and enforcing the same normalization value for MOS, and allowing the pn normalization to vary.

3. Morphological Parameters

In the following we introduce the methods for the substructure and morphology characterization.

3.1. Concentration

The concentration parameter indicates how concentrated the X-ray emission is and was first introduced by Santos et al. (2008) as a good indicator for the presence of cooling-core systems at high redshift. It is defined as the ratio of the emission within two different circular apertures. In this paper we use

$$c = \frac{\mathrm{SB}(<0.1R_{500})}{\mathrm{SB}(<R_{\mathrm{max}})}, \quad (4)$$

where R_{max} can be either $0.5R_{500}$ or R_{500}. While in papers using *Chandra* observations, it is possible to directly use the source counts estimated from the images, here we must take the *XMM-Newton* point-spread function (PSF) into account. Thus, we integrated the SB profiles deconvolved with the PSF. We discuss the relation between the concentration value obtained with and without the PSF correction in Appendix B.

3.2. Centroid Shift

The centroid shitft parameter is defined as the variance of the projected separation between the X-ray peak determined from the smoothed image (with a Gaussian of FWHM of 6 arcsec) and the centroid of the emission obtained within 10 apertures of increasing radius up to R_{max}:

$$w = \left[\frac{1}{N-1}\sum_i (\Delta_i - \overline{\Delta})^2\right]^{\frac{1}{2}} \frac{1}{R_{\mathrm{max}}}. \quad (5)$$

The default value for R_{max} is $0.5R_{500}$, but when R_{500} fits completely within the FOV, we also estimated the values at $R_{\mathrm{max}} = R_{500}$.

3.3. Power Ratios

Introduced by Buote & Tsai (1995), the power-ratio method is motivated by the idea that the SB is a good representation of the projected mass distribution of the cluster. The power ratios consist of a 2D multipole decomposition of the surface brightness distribution within a specified aperture, and they account for the radial fluctuations where the high-order moments are sensitive to increasingly smaller scales.

The m-order power ratio is defined as P_m/P_0,with

$$P_0 = [a_0 \ln(R_{\mathrm{ap}})]^2 \quad (6)$$

$$P_m = \frac{1}{2m^2 R_{\mathrm{ap}}^{2m}}(a_m^2 + b_m^2), \quad (7)$$

where a_0 is the total intensity within the aperture radius R_{ap}. The moments a_m and b_m are calculated by

$$a_m(R) = \int_{R<R} S(x) R^m \cos(m\phi) d^2x \quad (8)$$

and

$$b_m(R) = \int_{R<R} S(x) R^m \sin(m\phi) d^2x, \quad (9)$$

where $S(x)$ is the X-ray surface brightness at the position $x = (R, \phi)$. In this paper we focus on the third (i.e., P3/P0, hereafter P30) and fourth (i.e., P4/P0, hereafter P40) moments, which are sensitive to the large-scale and small-scale substructures.

3.4. Gini Coefficient

The Gini coefficient, a standard economic measure of income inequality, was used for the first time in astronomy by Abraham et al. (2003) to measure the light concentration of all galaxy types and characterize their morphology. In this paper we use it as a measure of the X-ray flux distribution in galaxy clusters. If the total flux is equally distributed among the considered pixels, then the Gini coefficient is equal to 0, while if the total flux is concentrated into a single pixel, then its value is equal to 1. We adopt the definition from Lotz et al. (2004):

$$G = \frac{1}{|\bar{K}|n(n-1)}\sum_i (2i - n - 1)|K_i|, \quad (10)$$

where K_i is the pixel value in the ith pixel of a given image, n is the total number of pixels, and $\bar{K}$ is the mean of the absolute values of all n pixels in the image. As discussed by Lotz et al. (2004), the absolute values of k_i are required because in the low surface brightness regions, some pixels can result in negative values after the background subtraction. Including these negative values can yield a Gini coefficient to achieve values higher than 1. We note that the Gini coefficient is less sensitive to surface brightness effects and does not require a well-defined centroid (i.e., whether the flux is concentrated in a few pixels in the center or in the outer regions, the obtained value is the same). This makes this parameters interesting for distant clusters and shallow observations that do not allow a precise determination of the X-ray peak. To our knowledge, only Parekh et al. (2015) computed this parameter to X-ray observations of galaxy clusters.

3.5. Central Electron Density

While the formation of a cool core in the ICM is not a fully understood process, many studies (e.g., Hudson et al. 2010) have shown that the most relaxed systems tend to have a high gas density core with no significant redshift evolution (e.g., McDonald et al. 2017). Under the assumption of spherical symmetry, the gas density profile can be obtained from the combination of the best-fit results from the spectral and imaging analyses, as described in Lovisari et al. (2015) (see also Hudson et al. 2010). In this paper we use the value of the density computed at $0.02R_{500}$ to avoid the problem of modeling close to $R = 0$ (where the density profile may diverge), but still close enough to the cluster center to be representative of the central electron density. The central densities have not been scaled by $E(z)^{-2}$, but given the small redshift range, the impact on the values is modest.

3.6. Cuspiness

Related to the density profile, the cuspiness was suggested by Vikhlinin et al. (2007), and it is defined as

$$\alpha = -\frac{d\log\rho_g}{d\log r}, \quad (11)$$

where ρ_g is the gas density profile, and the function is computed at a fixed scaled radius of $0.04R_{500}$. This radius was chosen to be close enough to the core for the effect of cooling to be strong, but far enough away to avoid the flattening of the profile due to the outflows from the central AGN. We note that although for the SB profiles we removed most of the substructures, there are still a few cases where the fit is not perfectly in agreement with the data points, which might bias the cuspiness for some of the clusters (in particular the most disturbed ones).

3.7. Ellipticity

Although not necessarily a measure of substructures, the ellipticity is commonly defined by the ratio between the semiminor and semimajor axis. A measure of the ellipticity can also be obtained by the power ratio P2/P0. Although we verified that the two measurements are well correlated, in this paper we used the first definition.

4. Results

Of the 150 analyzed clusters (excluding clusters with completely flared observations), 120 clusters have R_{500} completely within the *XMM-Newton* FOV. For 28 clusters, the estimated R_{500} extends beyond the FOV, but we could still measure their properties within $0.5R_{500}$. Two of the analyzed objects (AWM7 and A1060) are very nearby, and therefore only a small fraction of their radius (i.e., $<0.3R_{500}$) lies within the FOV. Therefore we excluded them from the analysis. Thus, when plotting the parameters determined within R_{500}, we only use 120 objects, while when we investigate the properties at $0.5R_{500}$, we make use of the full sample of 148 objects. The subsample of objects observed with *XMM-Newton* is representative of the full sample in terms of total masses (see the *top* panel of Figure 1). The same is true for the objects fitting the *XMM-Newton* FOV, although the full sample includes a tail of low-mass objects. In the *bottom* panel of Figure 1, we also show the Planck mass-redshift distribution of the objects in the ESZ sample and the *XMM-Newton* coverage.

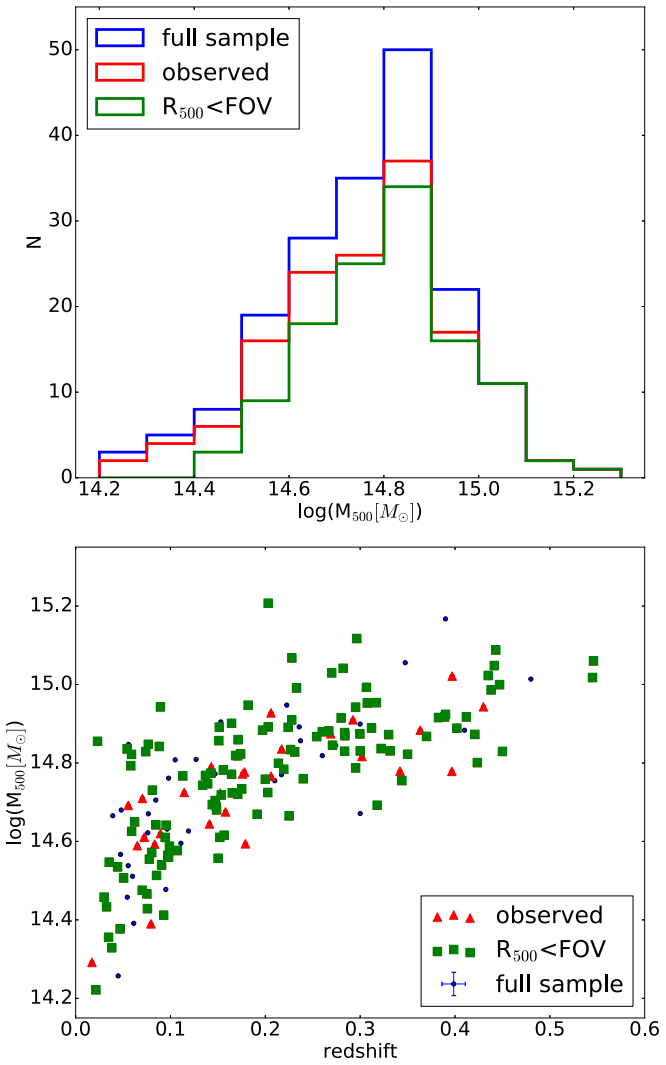

Figure 1. Top: distribution of the Planck cluster masses within R_{500} for the ESZ sample. The blue histogram refers to all the 188 objects, the red histogram to the clusters observed with *XMM-Newton* (excluding the flared observations), and the green histogram to the clusters that completely fit within the *XMM-Newton* FOV. Bottom: mass-redshift distribution for the ESZ sample with the same colors as in the top panel.

4.1. Morphology Parameters

The results of the substructure analysis is summarized in Figure 2, where we report the distribution of the parameters calculated within R_{500} (see Appendix C for the parameters calculated within $0.5R_{500}$). The uncertainties of the morphological parameters obtained directly using the images (i.e., Gini coefficient, centroid shift, power ratios, and ellipticity) have been obtained via Monte Carlo simulations, as previously done by Cassano et al. (2010) and Donahue et al. (2016). For every cluster we simulated 100 versions of the X-ray images by resampling the counts per pixel according to their Poissonian error. Similarly, to obtain the uncertainties of the parameters associated with the profiles (i.e., n_e, cuspiness, and concentration), we randomly varied the observational data points of the SB profiles 100 times to determine a new best fit. Again, the randomization was driven from the Gaussian distribution with mean and standard deviations in accordance with the observed data points and the associated uncertainties. Except for the power ratios, the uncertainties are very small (see Table 6) and are not expected to play a great role in the correlations and classification scheme for which we used only the parameter values. Thus, the errors have been used only for illustration purposes.

Although the different plots show a significant intrinsic scatter, the expected correlation between several parameters can still be observed. In fact, large centroid shifts and high power-ratios, as well as small X-ray concentrations, Gini coefficients, and low central densities are likely associated with disturbed clusters, and so these measurements are expected to correlate with each other. The strongest correlations (see Table 7 in Appendix I) have been obtained by comparing parameters that are more sensitive to the core properties, for example, c–n_e ($\rho = 0.87$ and $r = 0.87$), c–Gini ($\rho = 0.71$ and $r = 0.71$), or Gini–n_e ($\rho = 0.66$ and $r = 0.73$). A good correlation is also obtained when comparing parameters that are more sensitive to the level of substructures, e.g., w–P30 ($\rho = 0.63$ and $r = 0.53$), w–$P40$ ($\rho = 0.61$ and $r = 0.45$), or P30–P40 ($\rho = 0.99$ and $r = 0.56$). A weaker correlation is instead found when comparing a parameter that is sensitive to the core properties with one parameter sensitive to the level of substructures (e.g.,n_e–w ($\rho = -0.29$ and $r = -0.42$), c–$P30$

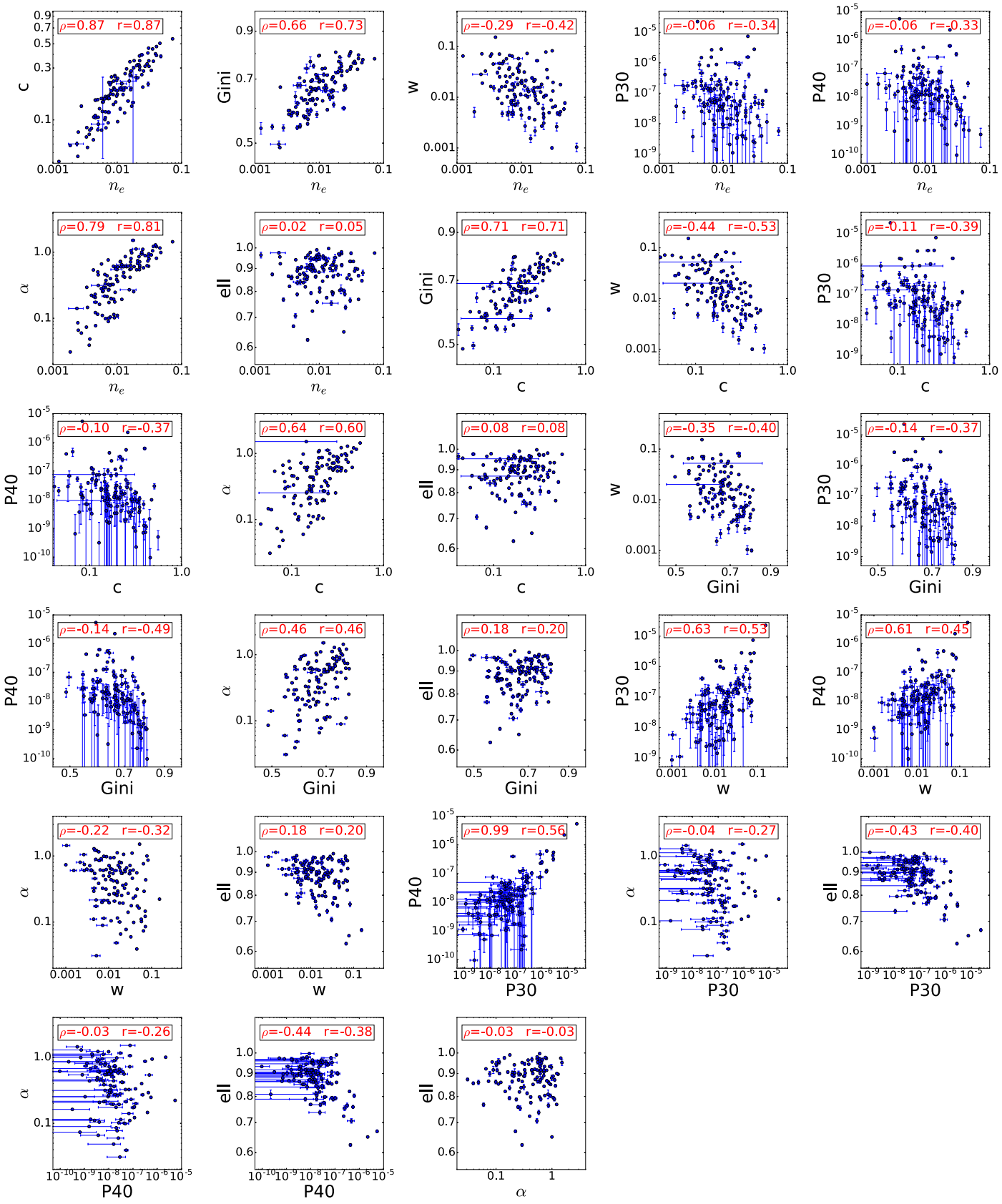

Figure 2. Parameters obtained within R_{500} plotted in the parameter-parameter planes. Here we show only the 120 galaxy clusters that have R_{500} completely within the *XMM-Newton* FOV. The ρ and r values indicate the Pearson and Spearman correlation coefficient (note that r is computed on ranks and so characterizes monotonic correlations, while ρ is computed on true values and characterizes linear correlation). Some of the parameters show a clear and strong correlation, while others are much more scattered.

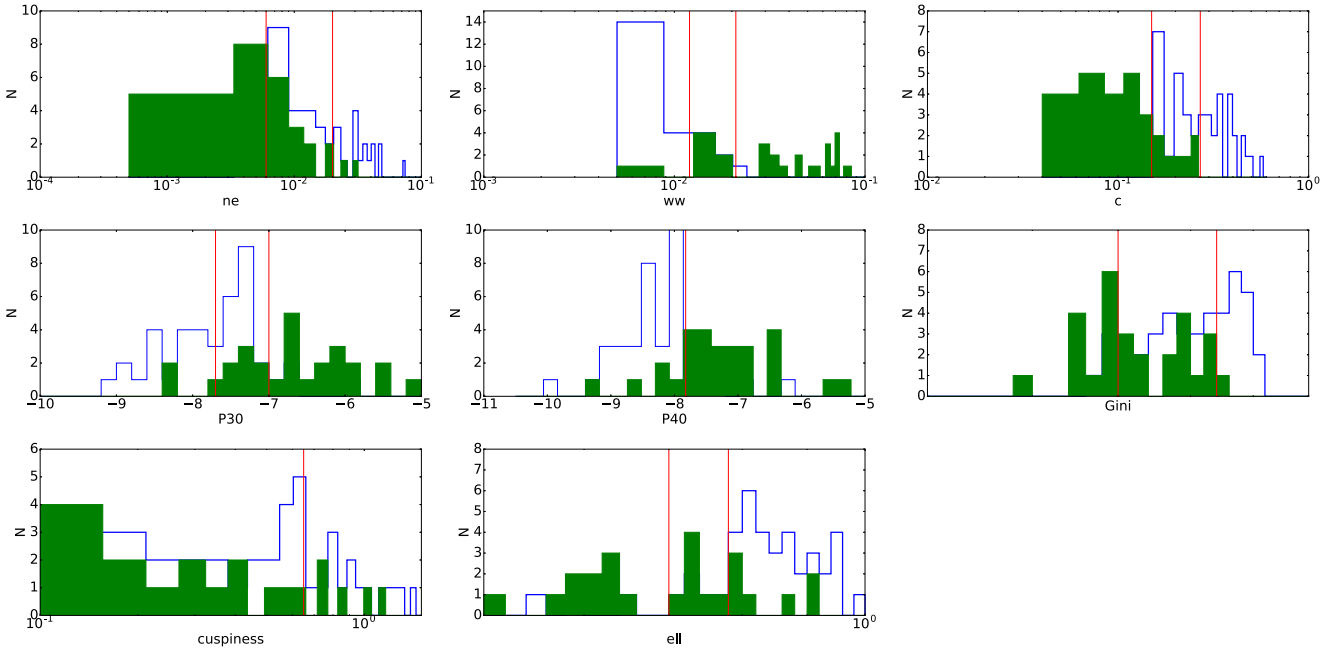

Figure 3. Distribution of the relaxed (blue) and disturbed (green) systems as a function of the different parameters. The vertical red lines represent the limit values used in Tables 2 and 3. To highlight the difference between relaxed and disturbed systems, the mix objects are not plotted.

($\rho = -0.11$ and $r = -0.39$), or Gini–P40 ($\rho = -0.14$ and $r = -0.49$)).The ellipticity, while showing no correlation with the parameters sensitive to the core properties, correlates with the parameters that are sensitive to the level of substructures.

4.2. Finding the Most Relaxed and Most Disturbed Objects

Each parameter has a different ability to distinguish between relaxed and unrelaxed systems. To evaluate each parameter's ability in determining the dynamical state, we follow a procedure presented by Rasia et al. (2013), where the clusters are visually classified as relaxed, disturbed, and "mix." A group of six astronomers inspected the images and rated the relaxation[7] state of the clusters with a grade that ranges from 1 (most relaxed) to 4 (most disturbed). We then averaged the results. All the clusters with an average grade lower than 2 were classified as relaxed, while the clusters with an average grade higher than 3 were classified as disturbed. We refer to the remaining clusters with grades from 2 to 3 as mix. Although the classification is subjective, broadly speaking, objects with circular X-ray isophotes and without substructures are classified as relaxed, double or complex objects with clear evidence of merging are classified as disturbed, and all the other with small substructures or relatively flat X-ray distribution as mix objects (see the cluster images in Appendix G). The distribution of relaxed and unrelaxed objects is significantly shifted with little overlap for the centroid shift, concentration, and power-ratio parameters (see Figure 3). The overlap is larger for the central density, Gini, cuspiness, and ellipticity. For these latter parameters, choosing a threshold value to classify the objects will lead either to a contaminated or to an incomplete sample. By "contaminated" we mean that some of the disturbed systems will be classified as relaxed (or the reverse), while for "incomplete," we mean that some of the relaxed objects are not recognized. If two distributions were to completely shift apart, then one could choose the threshold value that allows to have a complete and not contaminated sample. However, since all the histograms overlap, one needs to find a good compromise between the completeness of the sample and its contamination. Following Rasia et al. (2013), we define two properties, the sample completeness "C" and the purity "P":

$$C_r = \frac{\mathrm{QN(relaxed)}}{\mathrm{TN(relaxed)}} \tag{12}$$

$$P_r = \frac{\mathrm{QN(relaxed)}}{\mathrm{QN(relaxed + disturbed)}}, \tag{13}$$

where QN is the number of objects above (or below) a certain threshold and TN is the total number of objects. In a similar way, we computed C_d and P_d for the disturbed objects. We also provide the purity of the sample when mix objects are also considered:

$$P_{\mathrm{ext}} = \frac{\mathrm{QN(relaxed)}}{\mathrm{QN(relaxed + disturbed + mix)}}. \tag{14}$$

In Table 1 we summarized the results of the analyses where we searched for the threshold values that optimize either C or P. The two cluster parameters that perform better to select the relaxed systems are the concentration and the centroid shift, which for a completeness of 100% both have a purity of 84%. The centroid shift performs better than the concentration when one searches for high purity (e.g., $P > 95\%$). In fact, the high purity for the concentration is reached at the higher detriment of the completeness than for the centroid shift. The selection of the most disturbed objects is more difficult than for the relaxed objects. The reason is probably that parameters that depend on models, like c or n_e, are better determined for relaxed than for disturbed clusters. The clusters marked as disturbed but showing a rather high concentration (see Figure 13) are usually

[7] Although the morphological disturbance (especially in 2D) is not directly equivalent to a departure from relaxation, as quantified for instance by the $E_{\mathrm{kinetic}}/E_{\mathrm{thermal}}$ ratio, here we refer to clusters with a low level of substructures.

Table 1
For Each Parameter, We Indicate the Limit (L) that Characterizes the Relaxed and Disturbed Systems and the Purity (P) and Completeness (C) Parameters

Par	Relaxed				Disturbed			
	L_r	C_r	P_r	$P_{\rm ext}$	L_d	C_d	P_d	$P_{\rm ext}$
n_e	>7.0e–3	0.97	0.74	0.45	<3.1e–2	1.00	0.49	0.27
n_e	>2.5e–2	0.32	0.92	0.71	<7e–3	0.54	0.94	0.39
w	<2.1e–2	1.00	0.84	0.48	>1.2e–2	0.96	0.79	0.40
w	<1.2e–2	0.82	0.97	0.60	>2.1e–2	0.75	1.00	0.51
c	>0.15	1.00	0.84	0.47	<0.27	1.00	0.61	0.31
c	>0.27	0.53	1.00	0.67	<0.15	0.75	1.00	0.60
Gini	>0.6	0.95	0.69	0.38	<0.75	1.00	0.54	0.27
Gini	>0.74	0.45	0.94	0.68	<0.60	0.43	0.86	0.46
P30	<2.0e–7	1.00	0.75	0.40	>2.0e–8	0.93	0.57	0.29
P30	<2.0e–8	0.47	0.90	0.58	>2.0e–7	0.54	1.00	0.63
P40	<5.0e–8	0.97	0.71	0.39	>5.0e–9	0.93	0.58	0.29
P40	<1.0e–8	0.68	0.87	0.65	>5.0e–8	0.46	0.93	0.54
cusp	>0.10	0.97	0.64	0.34	<1.00	0.93	0.44	0.24
ell	>0.84	0.97	0.67	0.40	<0.95	0.82	0.40	0.32

Note. $P_{\rm ext}$ refers to the purity calculated including the mix objects. For most of the parameters we provide two threshold values, one to optimize the completeness, and one to optimize the purity.

double or complex objects. For these clusters, only the main subscluster was used to calculate the concentration values, slightly overestimating the concentration.[8] The centroid shift is again found to be the best parameter for distinguishing the most disturbed from the most relaxed objects, but the purity of the sample is lower.

The different parameters are sensitive to different properties of the clusters. For example, power ratios and centroid shifts are sensitive to the presence of substructures, while the central density is more connected to the core properties of the clusters. Some objects, which are quite relaxed and peaked in the center with some infalling substructures, can therefore be classified differently when different parameters are used. One way to have a more robust selection of the most relaxed clusters in the sample is to combine more parameters. When combining two parameters, we wish to keep the completeness as high as we have done with one single threshold, but increase the purity of the sample. For example, for both concentration and centroid shift taken individually, the chosen thresholds give a 100% completeness, but "only" a 84% purity. Combining concentration and centroid shift, we obtain a purity of 97% while maintaining the full completeness. In general, adding a second parameter in the selection of the relaxed clusters always improves the purity of the sample, although for some, the completeness drops below 90%. In Table 2 we list only the best parameter combinations. The centroid shift removes unrelaxed objects from the sample very well. In fact, the purity of all the parameters increases by 10% or more when combined with w. The power ratios and ellipticity also help to increase the purity of the sample, although not as significantly as the centroid shift. This suggests that combining a parameter that is more sensitive to the level of substructures like w, P30, and P40 with parameters that are more sensitive to the core properties like n_e and c is the best way to identify the most relaxed clusters.

[8] We note that A2443, A2163, and PLCKESZ124.21-36.48 still show a concentration higher than 0.15 even when using the values that were directly derived from the images for which the PSF effect is not taken into account.

Table 2
For Each Parameter, We Indicate the Limit (L) that Characterizes the Relaxed and Disturbed Systems and the Purity (P) and Completeness (C) Parameters

Par			Relaxed		
	L_r		C_r	P_r	$P_{\rm ext}$
$c-w$	>0.15	<2.1e–2	1.00	0.97	0.59
$c-$ P30	>0.15	<2.0e–7	1.00	0.90	0.54
$c-P40$	>0.15	<5.0e–8	0.97	0.93	0.54
$c-P40$	>0.15	<2.0e–7	1.00	0.90	0.50
$c-$ ell	>0.15	>0.84	0.97	0.90	0.59
$c-n_e$	>0.15	>7.0e–3	0.97	0.86	0.51
n_e-w	>4.0e–3	<2.1e–2	1.00	0.88	0.51
P30 $-$ w	<1.0e–7	<2.1e–2	0.90	0.90	0.56
P30 $-$ $P40$	<1.3e–7	<5.0e–8	0.92	0.74	0.51
Gini $-$ c	>0.58	>0.15	1.00	0.86	0.48
Gini $-$ w	>0.62	<2.1e–2	0.95	0.92	0.56
Gini $-$ P30	>0.62	<2.0e–7	0.95	0.92	0.48
Par			Disturbed		
	L_d		C_d	P_d	$P_{\rm ext}$
$c-w$	<0.27	>1.2e–2	0.96	0.90	0.44
n_e-w	<3.1e–2	>1.2e–2	0.96	0.84	0.42
P30 $-$ w	>2.0e–8	>1.2e–2	0.89	0.83	0.42
n_e-c	<3.1e–2	<0.27	1.00	0.61	0.31
Gini $-$ w	<0.75	>1.2e–2	0.97	0.88	0.49

Note. We list here only the parameter combination that gives the best results. As in Table 1 $P_{\rm ext}$ refers to the purity calculated including the mix objects.

Combining more than two morphological parameters usually reduces the completeness of the sample. For example, the only combination of three parameters that maintains the full completeness of relaxed clusters is $c > 0.15$, $w < 0.021$, and $P30 < 2E\text{-}7$. However, this removes only very few mix objects.

4.3. SZ versus X-Ray Selected Clusters

It is interesting to compare the results for the ESZ clusters with those obtained with the REXCESS sample, which was designed to be representative of any high-quality local X-ray survey. The REXCESS clusters have been selected by their X-ray luminosity only without any specific requirement on their morphology or dynamical state. In the cumulative plots shown in Figure 4, we clearly see that Planck-selected objects tend to be morphologically more disturbed than their X-ray counterparts. Low p-values of the Kolmogorov-Smirnov (KS) test confirm that the two samples have indeed a different X-ray morphology when the centroid shift ($D = 0.33$, $p \leqslant 0.01$), concentration ($D = 0.36$, $p \leqslant 0.01$), or the cuspiness ($D = 0.31$, $p \leqslant 0.01$) is used. Instead, a p-value $= 0.75$ confirms that the two distributions are indistinguishable in terms of their central densities ($D = 0.13$). We give a possible explanation for this result in Section 5.3.

Since the REXCESS sample was obtained by applying two redshift cuts, to have a fairer comparison, we also selected from the ESZ sample only the objects in the redshift range 0.0564–0.183 (i.e., the same redshift range as the REXCESS clusters). We found no significant differences with respect to the results obtained using the full ESZ sample. The masses of the clusters in the ESZ sample are on average higher than those of the REXCESS sample, although there is little to no dependence of the morphological parameter values on cluster mass (see next section).

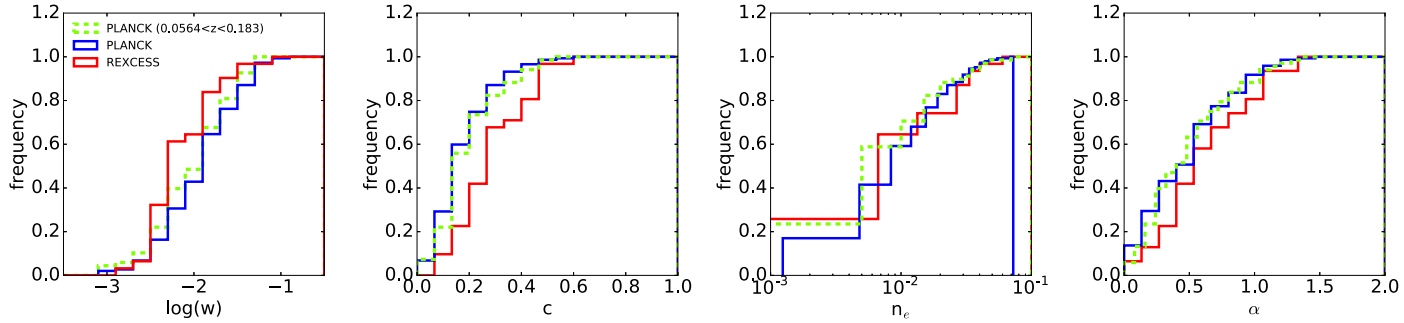

Figure 4. Comparison between the centroid shift (left), concentration (center-left), central density (center-right), and cuspiness (right) values for the ESZ (blue) and the REXCESS (red) samples calculated at R_{500}. The dashed green lines are the cumulative plots for the Planck clusters in the same redshift range as REXCESS. Indeed, the ESZ clusters are in general more disturbed than the REXCESS clusters.

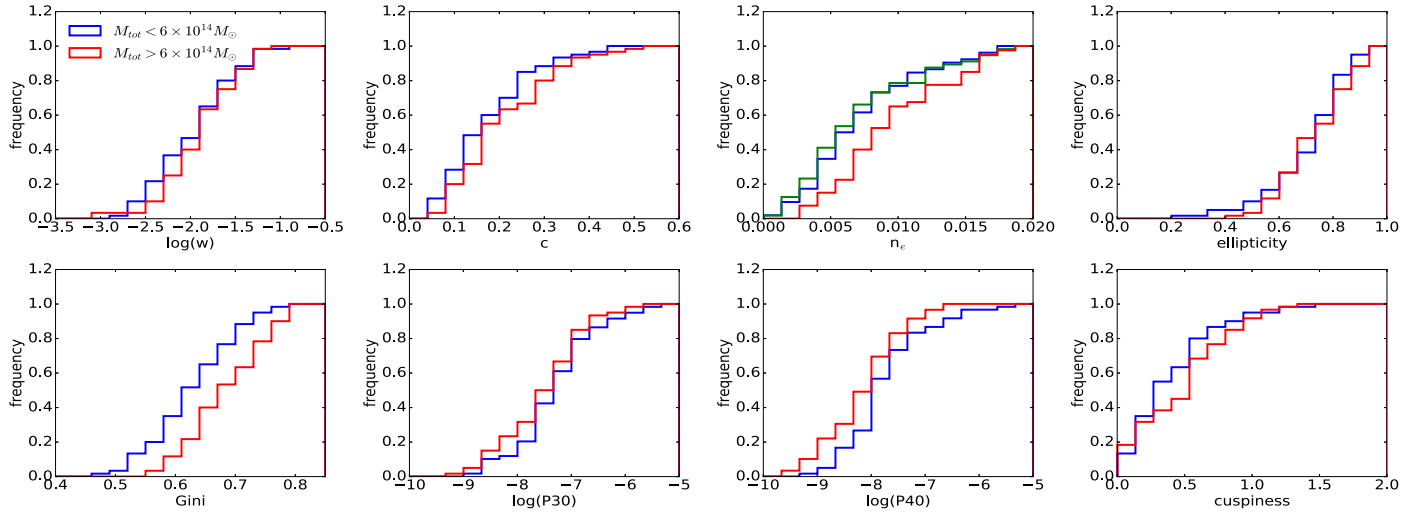

Figure 5. Comparison, from top left to bottom right panel, of the centroid shift, concentration, central density, ellipticity, Gini coefficient, P30, P40, and cuspiness values computed at R_{500} and subdividing the sample by the total mass.

4.4. Cluster Properties and Morphology

We investigated the dependence of the morphological parameters on different cluster properties like total mass and X-ray luminosity. The redshift dependence of the morphological parameters will be discussed in a forthcoming paper (i.e., J. Démoclès et al. 2017, in preparation).

We first investigated the variation of the morphological parameters with the total cluster mass (see Section 2.5 for the mass derivation), which is the most fundamental property for scaling relations of galaxy clusters. This also has some potential to affect the results obtained from comparing X-ray and SZ samples. In fact, the cluster mass distribution for X-ray selected samples usually extends to significantly lower masses than the SZ selected samples (e.g., Andrade-Santos et al. 2017).

In Figure 5 we show the cumulative plots for the morphological parameters computed within R_{500} (see Appendix C for similar plots computed within $0.5R_{500}$) when subdividing the sample into two mass bins to obtain a roughly similar number of objects in each subsample (note that the subsample with high-mass objects spans a broader range of redshift than the low-mass objects, which are more peaked at low redshift). We note that a p-value <0.01 of the KS test confirms that the subsamples of clusters with low and high masses are significantly different. Although there is a hint of a weak dependence of the centroid shift and the concentration on the cluster mass, this is not confirmed by means of the Spearman and Pearson tests, which give a relatively high probability of no correlation (see Table 3). We note that the Spearman test (which evaluates a monotonic relationship as

Table 3
Spearman and Pearson Rank Test Correlation and Probability for No Correlation between the Cluster Global Properties and the Morphological Parameters

	R_{500}			
Relation	r	p-value	ρ	p-value
M_{500}–c	0.04	0.69	0.07	0.43
M_{500}–w	0.05	0.61	0.04	0.63
M_{500}–n_e	0.27	<0.01	0.17	0.07
M_{500}–Gini	0.41	<0.01	0.36	<0.01
M_{500}–cusp	0.02	0.83	−0.03	0.72
M_{500}–P30	−0.15	0.10	−0.07	0.44
M_{500}–P40	−0.23	0.01	−0.08	0.38
M_{500}–ell	0.14	0.13	0.17	0.06
L_X–c	0.28	<0.01	0.22	0.03
L_X–w	0.01	0.91	0.04	0.68
L_X–n_e	0.49	<0.01	0.40	<0.01
L_X–Gini	0.52	<0.01	0.43	<0.01
L_X–cusp	0.20	0.04	0.17	0.09
L_X–P30	−0.09	0.37	−0.04	0.69
L_X–P40	−0.03	0.76	−0.18	0.07
L_X–ell	0.11	0.29	0.07	0.49

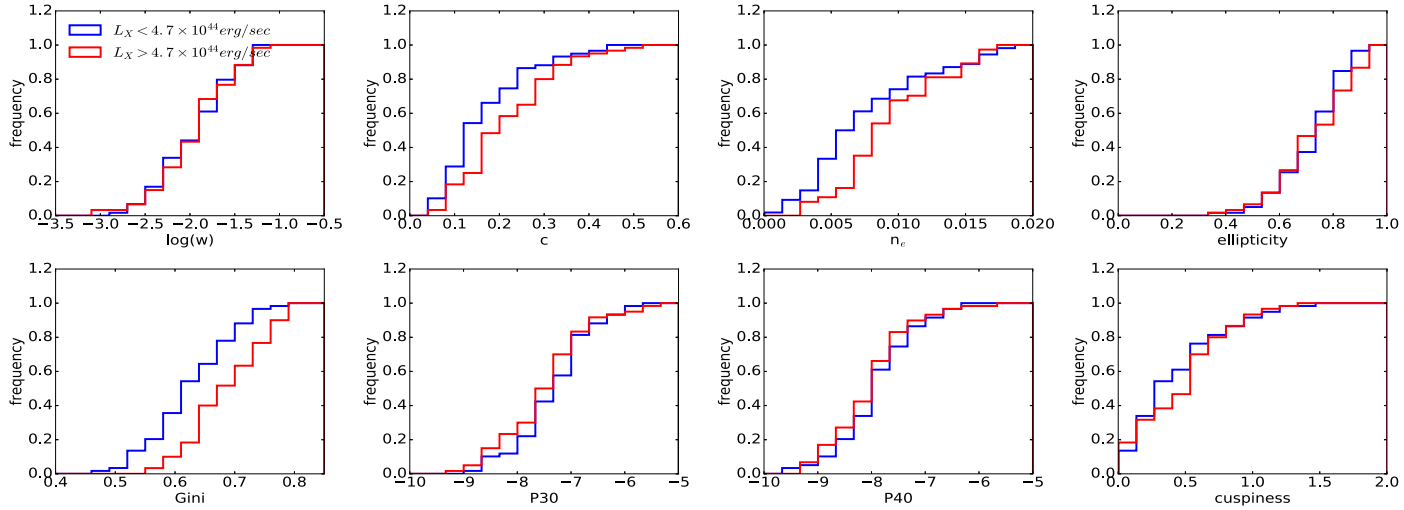

Figure 6. Comparison, from top left to bottom right panel, of the centroid shift, concentration, central density, ellipticity, Gini coefficient, P30, P40, and cuspiness values computed at R_{500} and subdividing the sample by the total luminosity.

opposed to the Pearson test, which evaluates a linear relationship) predicts a very weak correlation for the concentration. A dependence on the cluster mass is also observed with the central density, and in particular with the Gini coefficient, which shows a very strong correlation. More massive objects have higher values of the central density and the Gini coefficient. This trend with the total mass disappears ($r = 0.10$ and $\rho = 0.05$) when we consider the Gini coefficient computed within $0.5R_{500}$ instead of R_{500}.

In Figure 6 we show the cumulative plots for the same parameters when subdividing the sample by the cluster luminosities ($L_X = 4.7 \times 10^{44}$ erg s^{-1} gives a roughly similar number of objects in each subsample). As expected, we observe that the most luminous objects tend to have higher concentrations, Gini coefficients, and central gas densities. At the same time, we do not observe any correlation between the X-ray luminosity and the centroid shift (see Table 3). Again we note that a p-value <0.01 of the KS test attests that the subsamples of clusters with low and high luminosity significantly differ.

5. Discussion

5.1. Morphological Parameters

In the past years, several studies (e.g., Mann & Ebeling 2012; Mantz et al. 2015; Parekh et al. 2015) dealt with the classification of the galaxy clusters as relaxed or disturbed using different morphological parameters. Most of them are based on the analyses of *Chandra* data (e.g., Cuciti et al. 2015; Mantz et al. 2015; Parekh et al. 2015), which allow a good spatial resolution but provide only a small cluster coverage (at least in the low-redshift regime where relatively short observations allow a good data quality of the images and profiles). To our knowledge, the only study based on *XMM-Newton* data that dealt with such classification is the one by Böhringer et al. (2010), who performed an investigation of 31 clusters from the REXCESS sample. While the unprecedented spatial resolution of *Chandra* allows detecting small-scale substructures (but for most of the clusters we are limited by statistics), the advantage of *XMM-Newton* is of course its larger FOV, which allows determining the morphological parameters up to R_{500} even for relatively low-redshift objects, and its large effective area, which allows collecting many photons, which is necessary to derive the morphological parameters with a great accuracy. For instance, Bartalucci et al. (2017) showed that while *XMM-Newton* and *Chandra* measurements of the centroid shift are consistent even for high-redshift ($z \approx 1$) massive clusters, *XMM-Newton* yields about three times smaller uncertainties than *Chandra* for a given exposure time.

We presented a set of eight morphological parameters to constrain the dynamical state of the ESZ galaxy clusters. Three of them (i.e., centroid shift w and the two power ratios P30 and P40) are sensitive to the presence of substructures, which are certainly indicative of a dynamically active system. Since the absence of substructures does not necessary imply that the cluster is relaxed, we complemented the results with the concentration, central density, cuspiness, and Gini coefficient, which instead are more sensitive to the core properties (i.e., how peaked the gas distribution is, which is an indication of relaxation) of the systems. Finally, an old merger in which most of the substructures have been washed out can still be identify by the strong elliptical shape of the cluster.

Some of these parameters show a very strong correlation with each other (e.g., n_e–c or P30–P40), while others show no correlation (e.g., P30-cuspiness or Gini-ellipticity). This is true both within $0.5R_{500}$ and considering the full volume within R_{500}. The correlation is, not surprisingly, tighter when the two considered parameters are more sensitive to the core properties (n_e, Gini, and c) or, with somewhat weaker correlation coefficients, when the two considered parameters are more sensitive to the level of the substructures (e.g., w, P30). Instead, when two parameters sensitive to different features (i.e., one to the core properties and one to the presence of substructures) are considered, the correlation is much weaker. The reason is most probably that some clusters with infalling substructures still host a cool core in the center. Thus, on the one hand, the concentration, Gini coefficient, and central density suggest a more relaxed object, on the other hand, w, P30, and P40, which are more sensitive to the level of substructures, show a more disturbed dynamical state for the cluster. Nevertheless, almost all the correlations are quite scattered, which suggests that using one parameter alone to classify relaxed or unrelaxed clusters can yield misleading results.

The concentration, centroid shift, and, at a lower level, the power ratios are able to separate the distribution of relaxed and unrelaxed systems with very little overlap (see histograms in Figure 3). The other parameters (i.e., cuspiness, Gini coefficient, n_e, and ellipticity) instead show a large number of objects in the overlap region, making these parameters less powerful in distinguishing between different dynamical states. All the objects that are visually identified as relaxed have a concentration higher than 0.15 and a centroid shift smaller than 0.021. Using only one of these threshold values allows us to build a subsample of objects that includes all the relaxed systems with a 16% contamination of disturbed systems, which make them the parameters that are best suited to characterize the cluster dynamical state of the parameters we investigated in this paper. Indeed, the contamination is higher when the mix objects are included in the calculation. On the other hand, by definition, these objects do not show clear merging features, and they might also be relaxed.

The Gini coefficient strongly correlates with the concentration. This makes it very attractive, and in theory very powerful, because in contrast to the concentration, it is insensitive to the choice of the X-ray center. Unfortunately, our results show that the Gini coefficient is not as efficient as the concentration and/or the centroid shift in distinguishing the most relaxed from the most disturbed objects. One of the reasons is that double or complex objects (e.g., A2744 or PLCKESZ266.02-21.25), for which we should expect low Gini coefficients, show prominent substructures where the flux is concentrated, the effect of which is that the Gini values are increased. Conversely, some relaxed clusters (e.g., A2175 or A2426) have a surprisingly low Gini coefficient, probably due to the Gini definition used in this paper. In fact, as discussed in Section 3.4, we assigned a positive value to the pixels that scattered below the sky level. As explained by Lotz et al. (2004), this correction is not able to recover the "true" Gini coefficient for images with a low S/N. Thus, for galaxy clusters with relatively shallow observations and with very few photons in the outer regions, the Gini value can be underestimated. Despite this, by combining it with *w,* which easily identifies the most relaxed objects, *c*, or P30, we can obtain a cleaner sample of relaxed (disturbed) systems.

5.2. Most Relaxed and Most Disturbed Systems

Current and future surveys will provide us with very large galaxy cluster catalogs, making eventual visual classification difficult as well as prone to the observer-bias problems connected with visual classification. Thus, we searched for the best combination of parameters that will allow us to robustly identify the most relaxed and most disturbed systems in a sample. Naively, one aims to detect all, and only the relaxed or disturbed objects. We showed that combining the concentration and centroid-shift values allows us to obtain all the relaxed (disturbed) objects with a very small contamination by merging (relaxed) systems. The power of this combination was also demonstrated by Cassano et al. (2010), who used these parameters to show the relation between galaxy cluster mergers and the presence of extended radio halos.

Following Rasia et al. (2013), we also define a new general parameter M as a combination of the concentration and the centroid shift. This allowed us to have one single value to classify the X-ray morphology, and to distinguish between the relaxed and disturbed systems. The definition of the parameter is the following:

$$M = \frac{1}{2}\left(\frac{c - 0.15}{c_{\rm quar} - c_m} - \frac{w - 0.021}{w_{\rm quar} - w_m}\right), \quad (15)$$

where c_m and w_m are the medians of the concentration and the centroid shift, respectively, and $c_{\rm quar}$ and $w_{\rm quar}$ are the first or the third quartile depending on whether the parameter of the specific cluster is smaller or larger than its median (see Rasia et al. 2013 for more details). In Figure 7 we show the distribution of the M values for all the clusters. The distribution clearly shifts apart for the relaxed and disturbed objects. All the relaxed objects have an M value greater than 0.5, while except for one cluster, all the disturbed objects have an M value lower than 0.5.

As an alternative to the centroid shift, one can use the power ratios, the ellipticity, or the central electron density, although their ability to remove the most disturbed or relaxed systems is lower than *w*. While in general combining more parameters always improves the purity of the sample, the best results are obtained when parameters more sensitive identifying substructures are combined with parameters more sensitive to the core properties. This is because some clusters, for which the core is still prominent (i.e., clusters that tend to give a high concentration), on large scales show the presence of substructures (e.g., infalling systems), which indicates that the system is not fully relaxed. Conversely, the bulk of the emission of some clusters appears to be relaxed on large scales (i.e., no presence of X-ray substructures), but at the same time, they do not show a bright and peaked core, suggesting that either an earlier merger prevented its formation or that the merger is ongoing along the line of sight, to which morphological parameters such as *w* are not very sensitive. Pruning these systems ensures that only the most relaxed objects are included in the sample.

While our results suggest that the centroid shift, possibly paired with a second parameter, is the most powerful parameter in distinguishing relaxed and disturbed systems, Parekh et al. (2015) suggested that unlike parameters that are sensitive to the core properties, parameters that are more sensitive to the substructures (like *w*) are not able to efficiently classify the dynamical stat of galaxy clusters. In particular, they investigate the smoothness and asymmetry parameters that Rasia et al. (2013) found very promising with simulations. Parekh et al. (2015) noted that the values of these two parameters depend on the cluster exposure time and S/N, which is also true for the power ratios, but not for the centroid shift (at least in the count regime investigated in this paper), as shown in Appendix A. So, while it is true that the ability of some parameters to distinguish different dynamical states indeed depends on the quality of the data, our results indicate that the centroid shift also works well in a relatively low-count regime.

The combination of different parameters to identify the most relaxed galaxy clusters from a sample was also used by Mantz et al. (2015), who introduced the symmetry-peakiness-alignment criterion. Their strategy was based on parameters that do not need a complete imaging coverage. However, they show that their parameters strongly (anti-)correlate with both concentration and centroid shift, suggesting that they are able to measure the same X-ray features. We note that although they use different parameters, they also combine a parameter more sensitive to the core properties (i.e., the peakiness) with

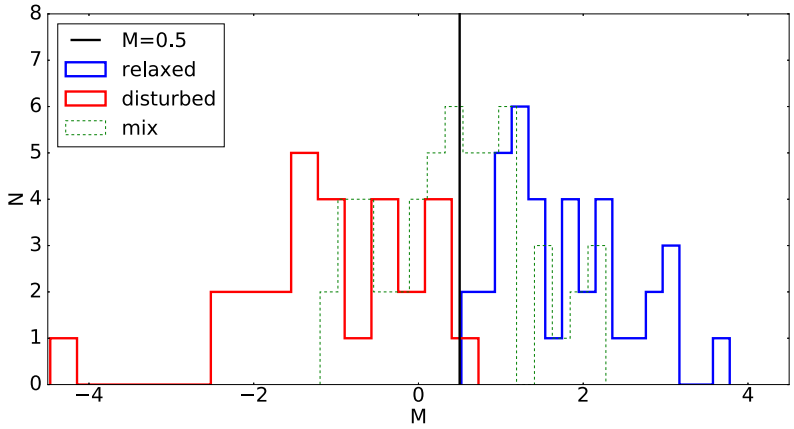

Figure 7. Distributions of the M parameter as defined in Equation (13). Blue and red histograms refer to visually classified relaxed and disturbed systems, while the dashed green distribution refers to the "mix" objects.

parameters more dependent to the large-scale inhomogeneities (i.e., symmetry and alignment), similarly to what we reported in this paper. We note that they restricted their analysis to relatively small radii, which may affect the final results (e.g., see the comparison between the parameters computed at $0.5R_{500}$ and R_{500} in Appendix C), and their analysis was optimized to find the most relaxed systems, while here we also provide threshold values for selecting the most disturbed galaxy clusters.

5.3. Dependence on the Cluster Properties

The hierarchical structure formation model predicts that massive clusters form through episodic mergers of low-mass units. Because of this, we might statistically expect to find the most massive objects in a more disturbed dynamical state. Our morphological analysis supports this scenario only when we use the central density or the Gini coefficient as the reference metric. The dependence of the central density on the cluster mass arises because the more massive clusters show a higher gas fraction (e.g., Pratt et al. 2009; Lovisari et al. 2015). The centroid shift and concentration parameters instead show no or a very weak dependence on the total mass. The correlation of the mass with the Gini coefficient is probably an artifact due to the change of the negative pixels in positive pixels that is required to avoid Gini values higher than 1, which would complicate the interpretation of the results. As discussed in the previous section (see also Appendix A), using absolute values may bias down the result of the Gini coefficient in low S/B regions. Thus, for low-mass clusters (and so less luminous clusters), the outer regions have a lower S/N (for a given exposure) and the Gini values will be biased down. When the outer regions are removed (e.g., when the parameters are computed within $0.5R_{500}$) from the calculation, and so most of the negative pixels are not included, the correlation between the total mass and the Gini coefficient disappears (see Table 5).

The mass dependence on the morphological parameter (centroid shift and power ratios) was also investigated by Böhringer et al. (2010). Their results also show no dependence of the morphological parameters on cluster mass. Rossetti et al. (2017) used the concentration parameter (but defined as the counts ratio within 40 and 400 kpc) to estimate the cool-core fraction for the Planck cosmology sample, subdividing the objects into two subsamples with different masses. They found hints of a higher cool-core fraction for the most massive objects, but at low significance. An indication of a higher cool-core fraction was also found by Mantz et al. (2015). McDonald et al. (2017) did not find any evidence of a redshift evolution in the fraction of merging clusters, which is consistent with an evolving merger rate (as predicted by the simulations of Fakhouri et al. 2010), provided that the relaxation timescale also evolves with redshift. Simulations have also shown that the merger rate has a weak dependence on halo mass (e.g., Fakhouri et al. 2010), but we argue that an infalling subhalo of a given mass would have a greater effect on a low-mass cluster than on a massive system (e.g., it will take longer to restore equilibrium). The fact that we do not observe major differences in the fraction of disturbed systems between low- and high-mass clusters supports the scenario suggested by McDonald et al. (2017), who proposed that halos assemble rapidly at high redshift and then the growth slows dwon. We note that our clusters do no span a very large range of masses, with 85% of them in the range 3–9 $\times$ 10^{14} $M_{\odot}$. So, the analysis should be extended to a larger range to confirm the current results.

Given the L_X–M relation, it is not surprising that there is also no correlation between the X-ray luminosity and the centroid shift, and power ratios. There is instead a weak correlation with the concentration. As noted by Böhringer et al. (2010), this is probably due to a selection effect. In fact, for a given mass, cool-core clusters have in general higher X-ray luminosities than non-cool-core clusters (Pratt et al. 2009). Since these cool-core clusters are usually more relaxed, they lie on the high-luminosity side.

As for the mass, we found that both central density and Gini coefficient are also correlated with the luminosity, which is expected given the L_X–M relation. The luminosity also shows a dependence on the concentration, with the most luminous having as expected a higher concentration in the center. Thus, the luminosity is indeed well correlated with parameters more sensitive to the core properties. It does not show any dependence on the parameters more connected with the presence of substructures. When we assume that the state of relaxation of a cluster is connected with the presence and number of substructures, then the X-ray global properties are not helpful to determine its dynamical state. A similar result was obtained with the REXCESS sample by Böhringer et al. (2010).

5.4. ESZ versus REXCESS

We compared different morphological parameters with those derived for the REXCESS sample. Except for the central density, all of them confirm that Planck-selected objects are generally more disturbed than the X-ray selected sample. Since the two samples have a different redshift distribution, and given the weak dependence on the redshift for some parameters, we also constrained the analyses to the same redshift range. However, the difference between the two samples remained. The two samples also have a different mass distribution, but as previously discussed, only the central density and Gini coefficient show a mass dependence, so this should not affect the comparison. The mass dependence of the central density is likely the explanation for the lack of difference between the ESZ and REXCESS values. In fact, ESZ clusters are more massive than REXCESS clusters, so they have in general a higher central density ($M_{\rm tot}$–n_e relation), but this is counterbalanced by the fact that the ESZ clusters are morphologically more disturbed and have a lower central density (e.g., $n_e - w$, $n_e - P_{30}$). This implies that if one uses the central density to compare the properties of SZ and X-ray selected samples, one must ensure that the samples span a similar range in redshift or total masses.

Recently, Rossetti et al. (2017) compared the fraction of cool-core clusters in the Planck cosmological sample and the X-ray selected sample MACS (Mann & Ebeling 2012) using the concentration parameter as a proxy for cool-cores. They found that the cool-core fraction in the X-ray selected sample is higher than in Planck. We note that their definition of c is taken from the original work of Santos et al. (2008) (i.e., $c = {\rm SB}(r < 40\,{\rm kpc})/{\rm SB}(r < 400\,{\rm kpc})$) and so is different from the definition we used in this paper.

The use of the different definitions for the concentration (i.e., using physical radii or a fixed fraction of R_{500}) might affect the determination of the specific fraction of cool-cores. In fact, McDonald et al. (2017) analyzed the density profiles of a large sample of clusters and suggested that the sizes of cool-cores are not evolving with time. According to this, it would make more sense to use physical instead of scaled radii to compute the concentration. On the other hand, Hudson et al. (2010) analyzed the temperature profiles of the HIFLUGCS sample (see Reiprich & Böhringer 2002 for more details) and showed that hotter (and so more massive) clusters have larger core radii (in physical scale), but these radii are in general smaller than $0.1R_{500}$ (used for example in this paper). Thus, while the sizes of the cores do not evolve, it is plausible that clusters of different masses host cores with different sizes, making both approaches suitable for these types of investigations. Andrade-Santos et al. (2017) compare the cool-core fraction in SZ and X-ray samples using both physical radii or a fixed fraction of R_{500}. Both methods point toward a larger number of relaxed objects in the X-ray selected samples, although the two approaches give a different fraction of cool-cores. The different fraction may depend on the threshold values used to classify a cluster as cool-core, but also on the fact that their sample span a broader range of masses.

Other studies (e.g., Mantz et al. 2015; Andrade-Santos et al. 2017; Rossetti et al. 2017) have shown that Planck-selected clusters tend to be morphologically more disturbed than their X-ray counterparts, in agreement with the fact that the selection of X-ray cluster samples is significantly biased toward cool-core clusters (e.g., Eckert et al. 2011; Andrade-Santos et al. 2017; Rossetti et al. 2017). The recent papers from Rossetti et al. (2017) and Andrade-Santos et al. (2017) computed several morphological parameters sensitive to the core properties (i.e., *c*, n_e, and *cuspiness*), and although a direct comparison is not possible because of the different definition of the parameters and of the used R_{500}, we note that our results qualitatively agree with their finding of a larger fraction of relaxed systems in the X-ray selected samples. However, contrary to what was found by Andrade-Santos et al. (2017), we did not find any significant difference in the central electron density of the Planck- and X-ray selected clusters. Of the different parameters computed in Andrade-Santos et al. (2017), the central electron density is the parameter that shows the smallest difference in terms of CC fraction between SZ and X-ray selected clusters. As we showed, more massive clusters have a higher electron density, so the comparison between the different samples depends on the relative mass distribution difference. Moreover, we note that Andrade-Santos et al. (2017) computed the central electron density at $0.01R_{500}$, while our values were computed at $0.02R_{500}$. Since the central density value is model dependent (i.e., the way one extrapolates to the center), the choice of R_{500} at which to compute n_e can partially explain the different results.

Previous studies that only considered X-ray data (e.g., Andrade-Santos et al. 2017; Rossetti et al. 2017) used parameters sensitive to the core properties to investigate the differences between X-ray and Planck-selected samples. In this paper, we confirmed that Planck-selected clusters tend to be morphologically more disturbed than their X-ray counterparts by using the centroid shift, which is more related to the dynamical state of the clusters than to their core properties. This result is in disagreement with what has been obtained by Nurgaliev et al. (2017), who did not find any morphological difference between an SPT sample and 400d, an X-ray selected sample (see Burenin et al. 2007 for more details). Indeed, the SPT sample is at $z > 0.4$, while the ESZ is at $z < 0.55$ (and mostly at much lower redshift), so maybe the difference is more important at low z. However, this raises the question about the origin of the difference between Planck and X-ray samples and/or why the SPT clusters do not show the same morphological differences. This will require a dedicated paper for which the parameters are estimated consistently (e.g., the same definition and the same algorithm for the parameter calculation) for well-defined and comparable samples (e.g., similar mass and redshift distribution).

6. Summary and Conclusion

In this paper we investigated several morphological parameters for the ESZ sample to identify which parameters are more powerful to determine the most relaxed objects from the sample. We also investigated whether the occurrence of substructures or the presence of cool cores depends on the cluster properties, incuding L_X and total mass. Finally, by comparing our results with what has been obtained with REXCESS data, a representative X-ray selected sample, we investigated whether the SZ and X-ray surveys select the same population of galaxy clusters. Our main conclusions are the following:

1. Concentration and centroid shift are the parameters that perform better in identifying relaxed systems. All the objects that were visually classified as relaxed have a concentration higher than 0.15 and a centroid-shift value lower than 2.1E-3.

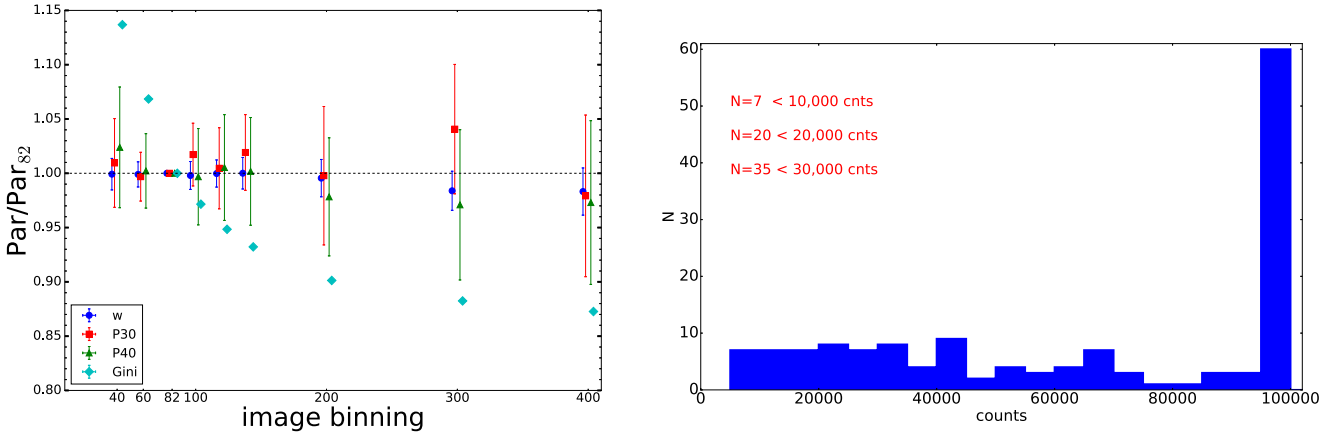

Figure 8. Left: relative change of the the centroid shift (blue), P30 (red), P40 (green), and Gini coefficient (cyan) for different image binnings with respect to the nominal binning (82 pixels, corresponding to $4\farcs1$). The image binning has little effect on all the morphological parameters, except for the Gini coefficient. Right: distribution of the galaxy clusters as a function of the number of counts within R_{500}. In the last bin we included all the objects with more than 100,000 counts. The legend reports how many objects are below a certain threshold.

2. Identifying the most disturbed systems by using the morphological parameters is in general more difficult than identifying the most relaxed systems.
3. Combining two parameters is a more efficient way to select a complete and pure sample of relaxed or disturbed systems. In particular, it is best to combine parameters that are more sensitive to substructures (e.g., w, P30, and P40) with parameters that are more sensitive to the core properties (e.g., n_e and c). The best results are obtained by combining the concentration with the centroid shift.
4. Except for the central gas density and Gini coefficient, there is no dependence on the morphological parameters with the total cluster mass. The $M_{\rm tot}$–n_e correlation implies that the central density can be used to compare different samples only if they span the same mass range.
5. Samples of SZ selected clusters tend to be more dynamically disturbed (i.e., high centroid shift and low concentration and central density) than the X-ray selected samples, in agreement with what has been found by other recent studies.

We thank the anonymous referee for the useful report that helped to improve the quality of the paper. We acknowledge Gerrit Schellenberger and Reinout van Weeren for helping with the visual classification of the clusters. L.L. acknowledges support from the *Chandra* X-ray Observatory grant GO3-14131X and by the *Chandra* X-ray Center through NASA contract NNX16AH31G. C.J. and W.R.F. are supported by the Smithsonian Institution. F.A.-S. acknowledges support from *Chandra* grant GO3-14131X. M.A., G.W.P., and J.D. acknowledge support from the European Research Council under the European Union's Seventh Framework Programme (FP7/2007–2013)/ERC grant agreement no. 340519.

Appendix A
Robustness of the Parameters

The clusters in our sample cover a large redshift range, so their extension on the sky varies from object to object, which might introduce systematic uncertainties in our measurements. In fact, for more distant objects, it might be harder to measure the small-scale substructures. Moreover, if the same image binning is used, for clusters at different redshift, we will probe a different physical scale. Furthermore, while some clusters have been observed with very long exposures, others have been observed with relatively short observations. This can introduce an uncertainty in the determination of the X-ray peak (in particular for the most unrelaxed objects) because of the poorer statistics, and it can reduce our ability to detect the smaller and fainter substructures.

In this section we describe the tests we performed to ensure that our results are stable and robust. First, we checked how important the choice of the image binnings is for the estimated parameters. Indeed, this choice has no effect on the parameters that are determined using the SB profiles (e.g., central density or concentration), but it may play a role for the parameters derived using the images. In Figure 8 we show the results for seven different binnings. The centroid shift, which basically is a measure of the flux distribution, is insensitive to the choice of the binning. This is very important when comparing clusters at different redshifts. The power ratios, which are a measure of the surface brightness inhomogeneities, were expected to be slightly more sensitive to the choice of the image binning. In particular, one would have expected to find lower values (i.e., more relaxed objects) when a higher binning is used, but the results in Figure 8 show that this is not the case and also that the power ratios are robust and independent of the choice of binning (if that would not have been the case, we would have found more relaxed objects at high redshift due to the different physical space probed by the same binning). The Gini coefficient instead shows a trend with the binning. In particular, increasing the binning leads to a lower Gini coefficient. The reason is that a larger binning tends to homogenize the flux distribution over the considered pixels. In fact, conceptually, the Gini coefficient is computed by ordering the pixels in ascending order by flux (or counts) and then comparing the resulting cumulative distribution to what would be expected if all the pixels had the same flux. So, when the flux difference from pixel to pixel is reduced, the cumulative distribution tends to deviate less from a perfectly even flux distribution. As a consequence of this and because we used a constant binning for our X-ray images, the obtained Gini factors for high-redshift clusters tend to be biased low with respect to the low-redshift objects.

To test whether the different exposures of the clusters in our sample can bias our results systematically, we recomputed the morphological parameters for all the objects reducing the

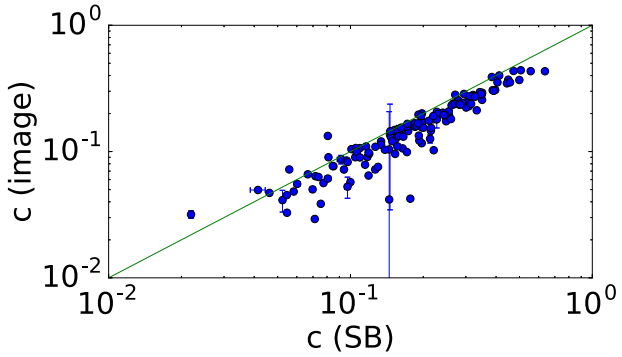

Figure 9. Comparison between the concentration values computed using the images and the SB profiles.

observation times by 50%, 80%, 90%, and 95%. Again, we found that the centroid shift is not sensitive to the quality of the data and the correct value can be recovered with relatively short observations. Indeed, the longer the observations, the smaller the statistical errors that are associated with the measurements. The power ratios are more sensitive to the number of source counts. For example, Weißmann et al. (2013) showed that relaxed clusters appear more disturbed when the number of counts is significantly smaller than 30,000 counts. In general, our clusters have a very good statistics, with only a few clusters with fewer than 10,000 source counts (see the histogram in Figure 8). Applying a counts cut to our sample does not improve the completeness and the purity of the sample significantly, however. For example, when we exclude all the objects with fewer than 30,000 counts, our completeness for P30 < 1E-7 increases from 90% to 93% and the purity from 79% to 84%.

We note that the X-ray peaks determined with a different fraction of the exposure time agree within a few arcsec for all the objects and that the scatter of the parameter values due to that difference in the uncertainty of the cluster center is negligible when compared with the error bars.

Appendix B
Comparison between the Concentration Values Obtained from the Images and SB Profiles

Because of the *XMM-Newton* PSF, the surface brightness of a cluster looks smoother than what it is in reality. In particular, the effect is stronger for the more distant objects because more photons originating in the center are spread out across much larger regions. As a consequence, using the *XMM-Newton* images leads to systematically lower concentrations for the more distant objects than for the low-redshift clusters. On the other hand, using the SB profiles might lead to some biases for the most disturbed systems because the clear substructures have to be removed to properly fit the profiles. Depending on the region where these substructures lie, the effect can be either to reduce or increase the concentration because of the lower number of counts within one of the two different circular apertures. In Figure 9 we show the comparison between the concentration used in the paper (i.e., c(SB)) and the concentration calculated from the images. Indeed, the correlation is good, and in general, SB profiles give a higher concentration because the PSF is taken into account. The correlation between the cluster global properties and the concentration computed with the images gives qualitatively the same results as when the SB profiles are used for the concentration (see Table 4).

Table 4
Spearman and Pearson Rank Test Correlation and Probability for No Correlation between the Cluster Global Properties and the Concentration Parameter Calculated Using the *XMM-Newton* Images

	R_{500}			
Relation	r	p-value	ρ	p-value
M_{500}–c	0.03	0.77	0.01	0.91
L_X–c	0.21	0.03	0.17	0.07
z–c	−0.17	0.06	−0.18	0.05

Appendix C
Cluster Properties and Morphology Parameters at $0.5R_{500}$

Clusters are continuously growing through accretion of lower-mass units. Substructures have been found to be relatively common in the outskirts of galaxy clusters (e.g., see the preliminary results of the *XMM-Newton* Cluster Outskirt Project, Tchernin et al. 2016; Eckert et al. 2017). As a consequence, the radius at which one computes the morphological parameters may assume a relevant role. Thus, if one limits the analyses to the innermost cluster regions (e.g., within $0.5R_{500}$), one might miss some of the infalling structures and mark a cluster as relaxed instead of disturbed.

In Figure 10 we compare w, c, g, and P30 calculated within $0.5R_{500}$ and R_{500} using only the clusters for which R_{500} fits within the FOV. Indeed, the concentration parameters show a very strong linear correlation (the Pearson rank test gives a correlation of 0.99), suggesting that the selection of clusters based on this parameter is not affected by a different radius (i.e., the clusters with a high concentration at R_{500} also have a high concentration at $0.5R_{500}$). This is due to the continuous and smooth shape of the SB profiles and to the fact that they are derived after the removal of all the visible substructures. The other parameters show a similar linear correlation (0.80, 0.77, and 0.55 for w, g, and P30, respectively), but are more scattered. Centroid shift and power ratios are more sensitive to the presence of substructures, and so the choice of the radius used for the calculation has a larger effect. In fact, the centroid shift measures the centroid variations in different aperture regions, so the presence of possible substructures in the region 0.5–$1R_{500}$ can dramatically change the centroid position for half of the considered apertures (i.e., the five apertures with $r \leqslant n \times R_{500}$, with $n = 6$–10). The same holds for the power ratios that are based on a 2D multipole expansion of the SB distribution (representing the mass distribution) and account for the azimuthal structures. The multipole moments are a measure for the substructures and depend on the distance to

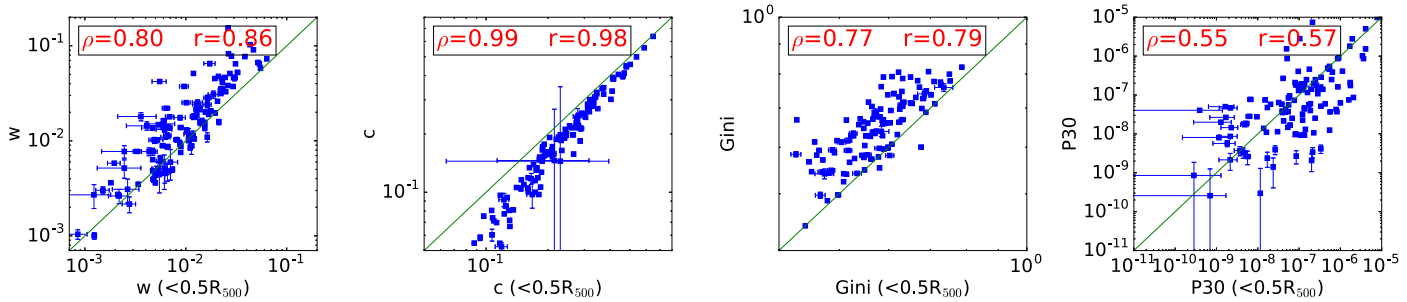

Figure 10. Comparison between the morphological parameters calculated within $0.5R_{500}$ and R_{500}. Note that for this comparison both w values have been renormalized by R_{500} (i.e., we divided the value of $w(R < R_{500})$ by two). The equality line is shown in green.

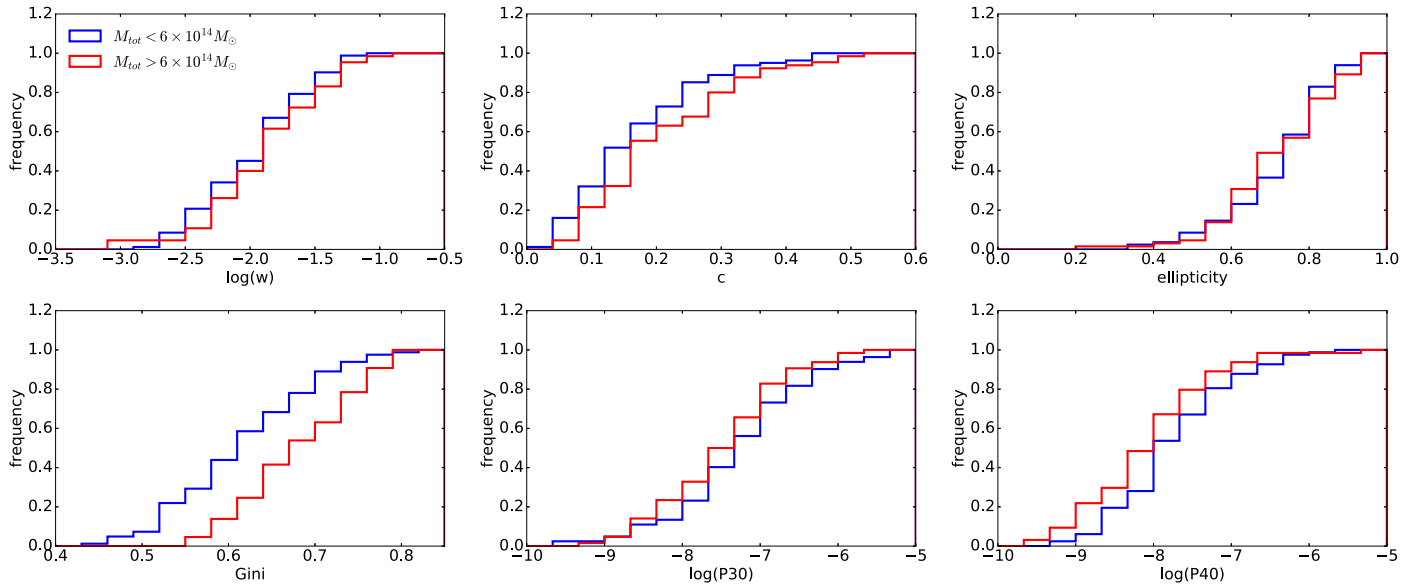

Figure 11. Comparison of the centroid shift (top left), concentration (top center), ellipticity (top right), Gini coefficient (bottom left), P30 (bottom center), and P40 (bottom right) values computed within $0.5R_{500}$ and subdividing the sample by the total mass.

Table 5
Spearman and Pearson Rank Test Correlation and Probability for No Correlation between the Cluster Global Properties and the Morphological Parameters Computed within $0.5R_{500}$

	$0.5R_{500}$			
Relation	r	p-value	ρ	p-value
M_{500}–c	0.09	0.27	0.03	0.70
M_{500}–w	0.07	0.38	0.14	0.09
M_{500}–n_e	0.28	<0.01	0.15	0.06
M_{500}–Gini	0.10	0.24	0.05	0.58
M_{500}–cusp	0.00	0.97	−0.05	0.59
M_{500}–P30	0.10	0.25	−0.07	0.41
L_X–c	0.28	<0.01	0.19	0.02
L_X–w	−0.04	0.63	0.05	0.59
L_X–n_e	0.50	<0.01	0.37	<0.01
L_X–Gini	0.22	<0.01	0.09	0.28
L_X–cusp	0.14	0.12	0.11	0.25
L_X–P30	−0.05	0.58	−0.09	0.25

the origin of possible substructures, as well as on their angular dependence, and since they are only sensitive to structures with a scale smaller than the considered aperture (see Buote & Tsai (1995) for more details about this last point), the choice of the radius at which P30 and P40 are calculated has an effect on the results. Considering a smaller region (e.g., $0.5R_{500}$ instead of R_{500}) leads to a smaller Gini coefficient because, as explained in Appendix A, all the low-flux pixels that strongly contribute to distancing the cumulative distribution from the even distribution are removed.

Despite the different parameter values at different scales, the parameter-parameter relations calculated at $0.5R_{500}$ are pretty similar to what was obtained at R_{500}. In Figure 13, we show the same plots as in Figure 2, but obtained within $0.5R_{500}$.

Similarly, when we compared the cluster properties with the morphological parameters computed within $0.5R_{500}$ (see Figures 11 and 12), we obtained qualitatively the same results (see Table 5) as discussed in Sections 4.4 and 5.3.

Appendix D
Relaxed versus Disturbed Clusters

In Figure 14 we show the distribution of the clusters visually classified as relaxed, "mix," and disturbed for the combination of parameters that better perform in distinguishing the most relaxed and most disturbed systems (see Table 2).

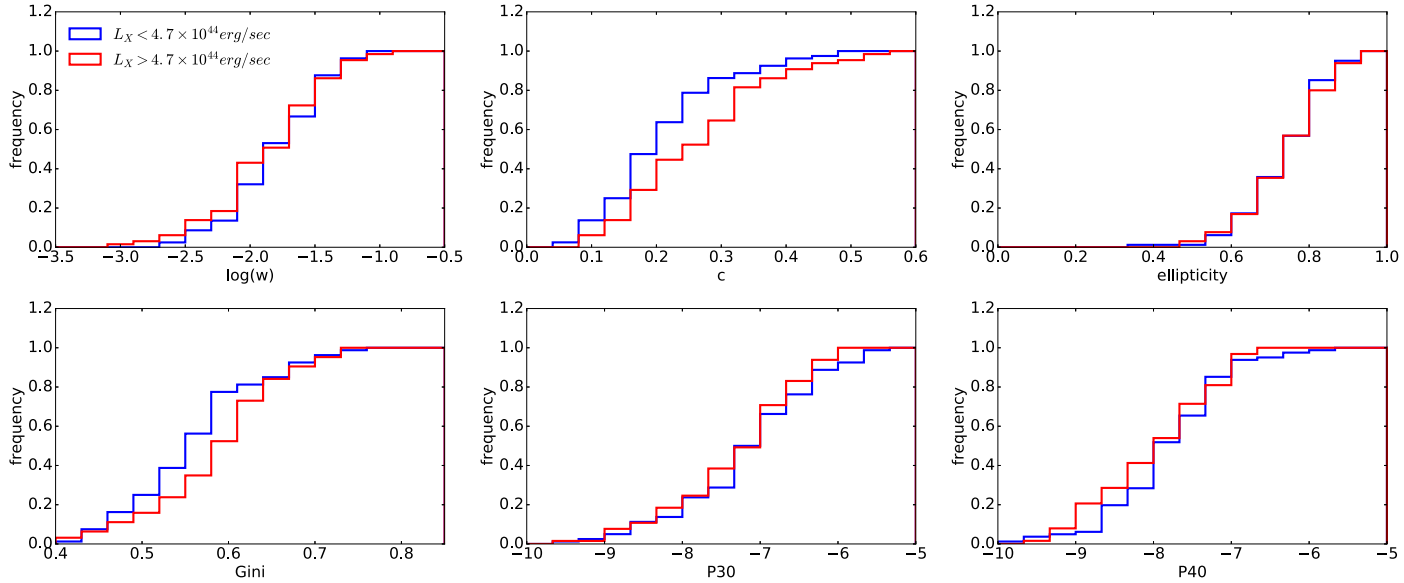

Figure 12. Comparison of the centroid shift (top left), concentration (top center), ellipticity (top right), Gini coefficient (bottom left), P30 (bottom center), and P40 (bottom right) values computed within $0.5R_{500}$ and subdividing the sample by the total luminosity.

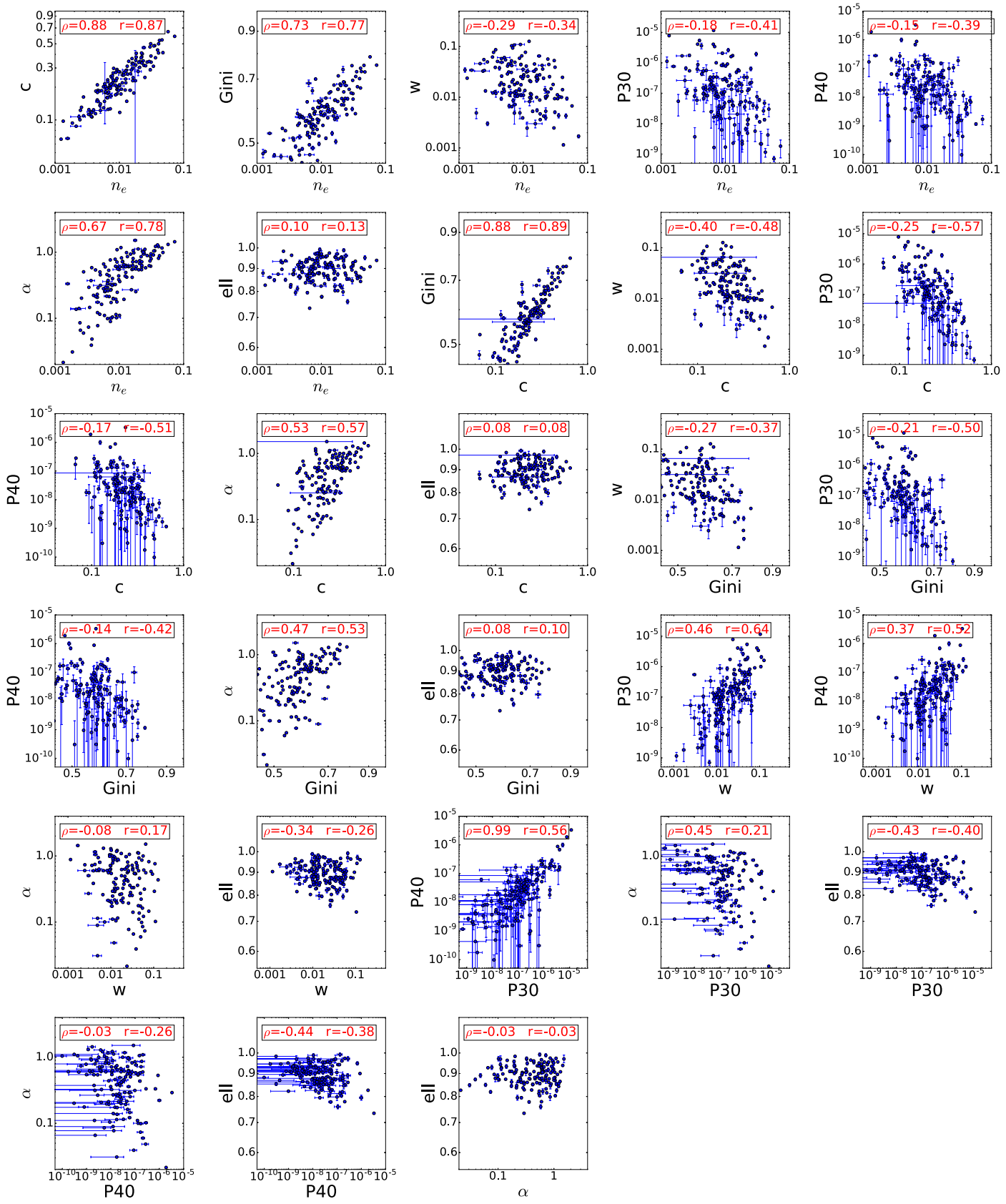

Figure 13. Parameters obtained within $0.5R_{500}$ plotted in the parameter-parameter planes. ρ and r values indicate the Pearson and Spearman correlation coefficient (note that r is computed on ranks and so characterizes monotonic correlations, while ρ is computed on true values and characterizes a linear correlation). Some of the parameters show a clear and strong correlation, while others are much more scattered.

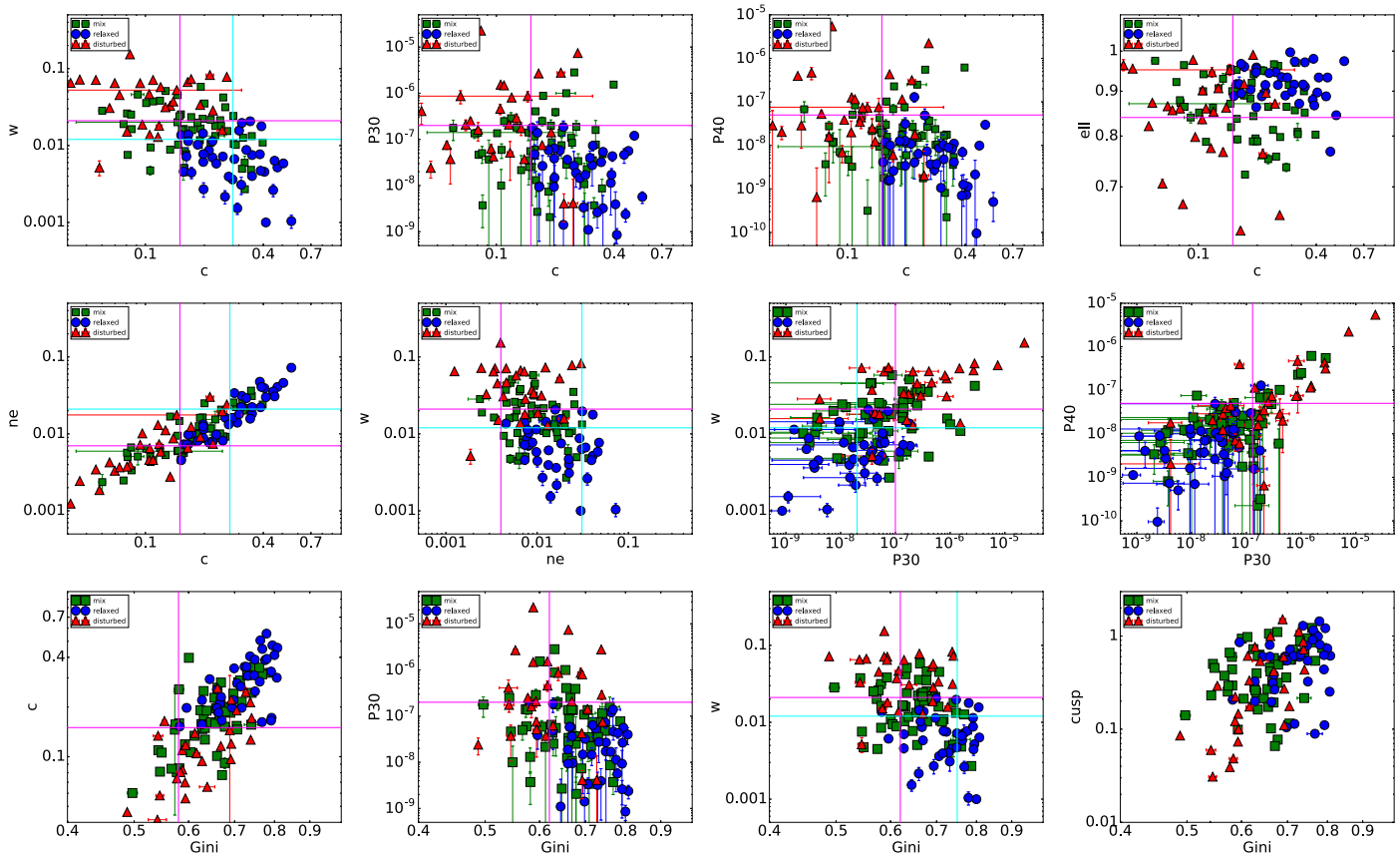

Figure 14. Distribution of the relaxed (blue), "mix" (green), and disturbed (red) clusters as a function of the different morphological parameters. The magenta and cyan lines represent the threshold values listed in Table 2 that were used to compute the completeness and the purity of the samples.

Appendix E
Visual Classification

The visual classification, in addition to being subjective, might also depend on other criteria, for example, the goodness of the images. We performed a few tests to ensure that our visual classification is robust.

First of all, we checked whether the same clusters are rated similarly when shown a second time to the six astronomers. This was done by showing the same images for 20 clusters several times, randomly chosen and displayed in a random order. All the 20 clusters have been classified in the same way (i.e., relaxed, "mix," and disturbed) with an average dispersion around the mean of 0.25. In particular, the most relaxed and most disturbed (i.e., the clusters with an average grade lower than 2 and greater than 3) show a smaller dispersion (0.13) than the "mix" objects (0.37).

Indeed, the number of counts is also an important parameter when classifying the clusters. Some clusters have very good data quality, which facilitates spotting possible surface brightness features. Furthermore, the image treatment can also play an important role, for example, progressively oversaturating the central regions of a cool-core cluster may help to reveal more and more structures because the contrast in the outer regions starts to become more evident. To test whether these issues can bias the visual classification, a second image with a reduced number of counts was produced and/or the color contrast changed for 40 galaxy clusters (again randomly selected). The new images were produced to have 10 to 30 thousand source counts (corresponding, depending on the cluster, to 10%–50% of the original total number of counts). Again, we found a very good agreement between the averaged grade obtained with the reduced and total number of counts. The dispersion around the mean was 0.14. We note that for 62% of the objects the averaged grade is lower when the classification was made with a reduced number of counts, indicating, as we said, that a better data quality facilitates identifying possible substructures. Nonetheless, only two objects were classified differently from the result obtained with the total number of counts. Moreover, given their morphological parameter values, the qualitative results of the paper would not change because they would fall in the quadrants associated with the most relaxed clusters.

Appendix F
Correlation Plots between the Cluster Properties and the Morphological Parameters

The correlation plots between the morphological parameters and the total mass and luminosity are shown in Figures 15 and 16, respectively.

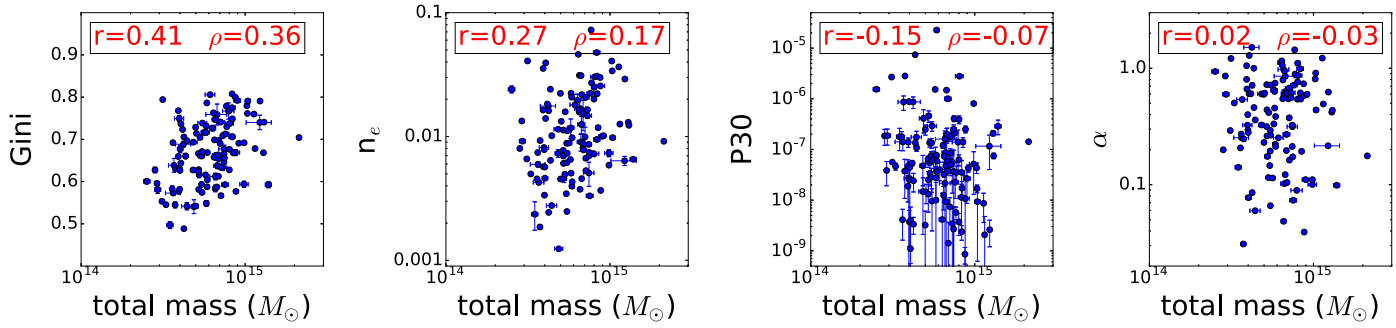

Figure 15. Correlations between the total mass and some of the morphological parameters computed within R_{500}. The correlation coefficient decreases from the left to the right.

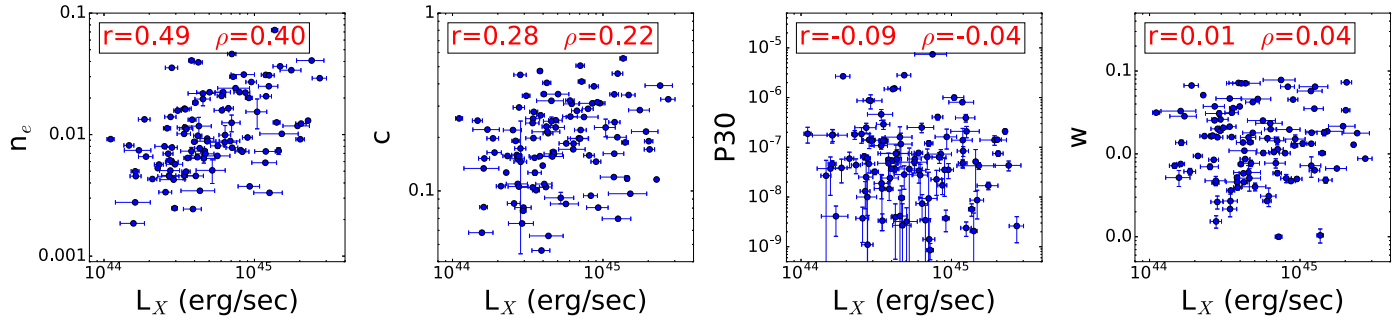

Figure 16. Correlations between the X-ray luminosity and some of the morphological parameters computed within R_{500}. The correlation coefficient decreases from the left to the right.

Appendix G
Cluster Images

Although the classification is subjective, broadly speaking, objects with circular X-ray isophotes and without substructures are classified as relaxed, objects without substructures but not perfectly circular X-ray isophotes (e.g., sloshing) are classified as semi-relaxed, objects with substructures but still with a well-formed cluster core (e.g., A85) are classified as semi-disturbed, and double or complex objects with clear evidence of merging are classified as disturbed. See the cluster images in Figure 17.

Appendix H
Parameter Values

All the parameter values used in this paper and calculated within R_{500} are listed in Table 6.

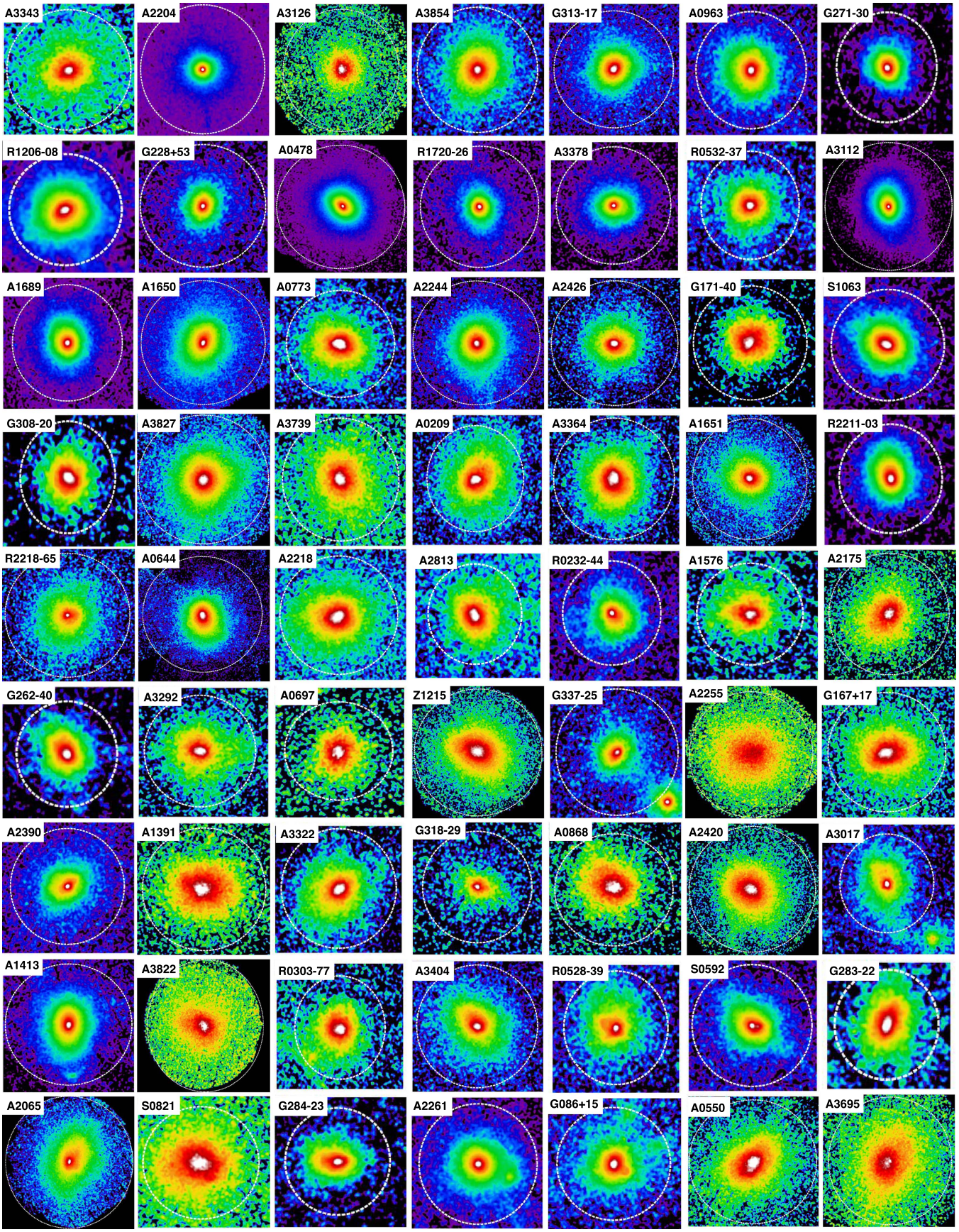

Figure 17. X-ray images of the galaxy clusters investigated in this paper, from the most relaxed to the most disturbed according to the visual classification. The white circles indicate the estimated R_{500}.

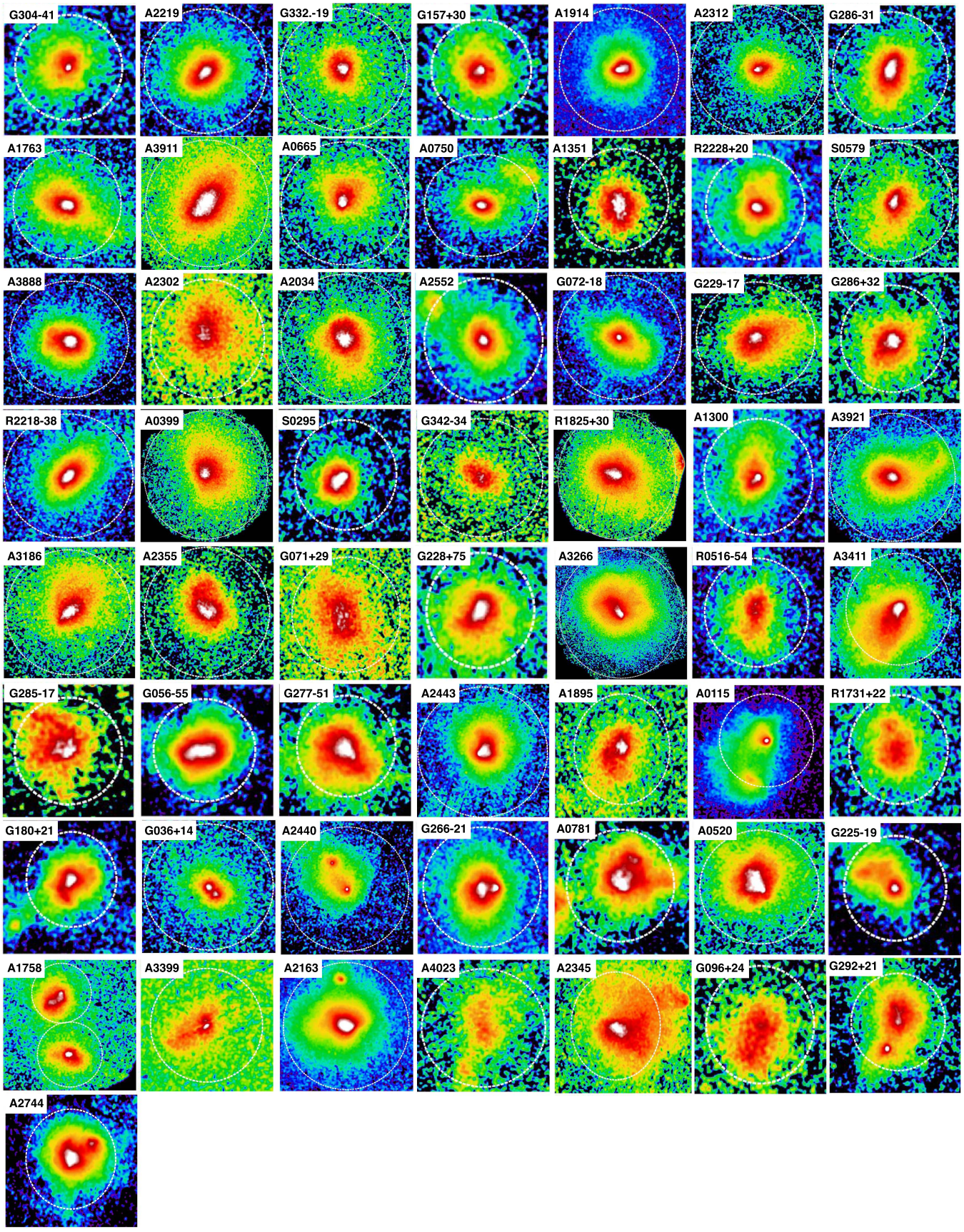

Figure 17. (Continued.)

Table 6
Morphological Parameters for the 120 Galaxy Clusters with R_{500} Completely Fitting within the *XMM-Newton* FOV

Planck Name	Alternative Name	R_{500} kpc	n_e $\times 10^{-2}$	cusp	c	w $\times 10^{-2}$	Gini	$P30$ $\times 10^{-7}$	$P40$ $\times 10^{-8}$	ell	Dynamical State
G000.44–41.83	A3739	1114	0.73 ± 0.05	0.33 ± 0.01	0.16 ± 0.01	0.46 ± 0.06	0.63 ± 0.01	0.48 ± 0.29	1.19 ± 0.93	0.92 ± 0.01	R
G002.74–56.18	RXCJ2218.6-3853	1106	1.01 ± 0.01	0.36 ± 0.01	0.24 ± 0.01	2.13 ± 0.04	0.70 ± 0.01	1.08 ± 0.16	1.66 ± 0.41	0.81 ± 0.01	M
G003.90–59.41	A3888	1270	0.99 ± 0.20	0.55 ± 0.01	0.18 ± 0.01	1.99 ± 0.03	0.69 ± 0.01	0.07 ± 0.04	1.21 ± 0.29	0.88 ± 0.01	M
G006.70–35.54	A3695	1065	0.57 ± 0.01	0.66 ± 0.01	0.08 ± 0.01	2.61 ± 0.05	0.58 ± 0.01	1.39 ± 0.29	2.75 ± 0.80	0.88 ± 0.01	M
G006.78+30.46	A2163	1817	0.92 ± 0.01	0.18 ± 0.01	0.19 ± 0.01	3.36 ± 0.01	0.70 ± 0.01	1.42 ± 0.04	11.40 ± 0.27	0.99 ± 0.01	D
G008.44–56.35	A3854	1061	1.64 ± 0.01	0.80 ± 0.01	0.25 ± 0.01	0.22 ± 0.04	0.66 ± 0.01	0.19 ± 0.10	0.73 ± 0.32	0.92 ± 0.01	R
G008.93–81.23	A2744	1360	0.59 ± 0.01	0.11 ± 0.01	0.12 ± 0.01	5.74 ± 0.03	0.69 ± 0.01	8.05 ± 0.21	7.37 ± 0.36	0.85 ± 0.01	D
G021.09+33.25	A2204	1323	7.25 ± 0.03	1.44 ± 0.01	0.56 ± 0.01	0.10 ± 0.02	0.78 ± 0.01	0.06 ± 0.02	0.05 ± 0.03	0.97 ± 0.01	R
G036.72+14.92		1241	1.96 ± 0.24	1.12 ± 0.01	0.25 ± 0.01	1.58 ± 0.05	0.73 ± 0.01	0.04 ± 0.10	0.20 ± 0.53	0.87 ± 0.01	D
G039.85–39.98	A2345	1077	0.24 ± 0.01	0.09 ± 0.01	0.05 ± 0.01	7.19 ± 0.05	0.49 ± 0.01	0.24 ± 0.10	2.04 ± 0.68	0.95 ± 0.01	D
G042.82+56.61	A2065	1189	1.13 ± 0.01	0.72 ± 0.01	0.19 ± 0.01	1.66 ± 0.03	0.62 ± 0.01	0.65 ± 0.09	1.77 ± 0.35	0.84 ± 0.01	M
G046.08+27.18	RXCJ1731+22	1148	0.38 ± 0.01	0.05 ± 0.01	0.08 ± 0.01	1.51 ± 0.18	0.58 ± 0.01	1.62 ± 0.70	1.59 ± 1.45	0.86 ± 0.01	D
G046.50–49.43	A2420	1194	0.70 ± 0.01	0.44 ± 0.01	0.16 ± 0.01	0.85 ± 0.03	0.58 ± 0.01	0.13 ± 0.07	1.58 ± 0.57	0.91 ± 0.01	M
G049.20+30.86	RXJ1720.1+2638	1241	4.61 ± 0.01	1.16 ± 0.01	0.51 ± 0.01	0.58 ± 0.04	0.76 ± 0.01	1.20 ± 0.15	2.99 ± 0.61	0.84 ± 0.01	R
G049.33+44.38	A2175	1049	0.46 ± 0.01	0.21 ± 0.01	0.15 ± 0.01	1.36 ± 0.10	0.58 ± 0.01	1.78 ± 0.47	0.41 ± 0.60	0.89 ± 0.01	R
G049.66–49.50	A2426	1090	1.40 ± 0.01	0.60 ± 0.01	0.29 ± 0.01	0.15 ± 0.03	0.64 ± 0.01	0.01 ± 0.03	0.88 ± 0.48	1.00 ± 0.01	R
G053.52+59.54	A2034	1189	0.50 ± 0.01	0.12 ± 0.01	0.15 ± 0.01	1.60 ± 0.07	0.70 ± 0.01	1.36 ± 0.24	0.18 ± 0.22	0.90 ± 0.01	M
G055.60+31.86	A2261	1234	3.10 ± 0.01	0.95 ± 0.01	0.35 ± 0.01	1.33 ± 0.03	0.75 ± 0.01	0.48 ± 0.08	0.54 ± 0.16	0.85 ± 0.01	M
G055.97–34.88	A2355	1110	0.28 ± 0.01	0.06 ± 0.01	0.13 ± 0.01	3.29 ± 0.09	0.54 ± 0.01	1.75 ± 0.54	2.49 ± 1.63	0.77 ± 0.01	D
G056.81+36.31	A2244	1098	1.83 ± 0.01	0.60 ± 0.01	0.35 ± 0.01	0.75 ± 0.02	0.72 ± 0.01	0.54 ± 0.06	1.10 ± 0.18	0.91 ± 0.01	R
G056.96-55.07		1255	1.01 ± 0.01	0.60 ± 0.01	0.10 ± 0.01	1.87 ± 0.04	0.69 ± 0.01	0.42 ± 0.07	3.87 ± 0.41	0.80 ± 0.01	D
G057.26–45.35	RXCJ2211.7-0350	1334	4.07 ± 0.03	0.81 ± 0.01	0.39 ± 0.01	1.78 ± 0.04	0.78 ± 0.01	0.43 ± 0.10	0.13 ± 0.09	0.87 ± 0.01	R
G058.28+18.59	RXCJ1825.3+3026	1028	0.50 ± 0.01	0.50 ± 0.01	0.08 ± 0.01	0.76 ± 0.01	0.55 ± 0.01	0.46 ± 0.07	1.48 ± 0.31	0.87 ± 0.01	M
G062.42–46.41	A2440	998	0.66 ± 0.01	0.29 ± 0.01	0.16 ± 0.01	6.69 ± 0.06	0.55 ± 0.01	26.80 ± 1.03	43.00 ± 2.94	0.62 ± 0.01	D
G067.23+67.46	A1914	1334	2.00 ± 0.01	0.54 ± 0.01	0.32 ± 0.01	1.26 ± 0.01	0.77 ± 0.01	0.04 ± 0.02	0.08 ± 0.06	0.97 ± 0.01	M
G071.61+29.79		1039	0.19 ± 0.01	0.03 ± 0.01	0.06 ± 0.01	0.52 ± 0.11	0.54 ± 0.01	0.37 ± 0.27	2.88 ± 2.02	0.87 ± 0.01	D
G072.63+41.46	A2219	1475	1.26 ± 0.01	0.49 ± 0.01	0.19 ± 0.01	1.02 ± 0.05	0.68 ± 0.01	0.02 ± 0.03	0.34 ± 0.22	0.92 ± 0.01	M
G072.80–18.72		1249	1.64 ± 0.01	1.06 ± 0.01	0.20 ± 0.01	2.23 ± 0.04	0.66 ± 0.01	0.12 ± 0.06	7.53 ± 1.19	0.80 ± 0.01	M
G073.96–27.82	A2390	1492	3.65 ± 0.01	1.22 ± 0.01	0.35 ± 0.01	0.48 ± 0.04	0.76 ± 0.01	0.09 ± 0.05	0.36 ± 0.24	0.90 ± 0.01	M
G080.38–33.20	A2443	1053	0.74 ± 0.01	0.27 ± 0.01	0.22 ± 0.01	2.85 ± 0.02	0.69 ± 0.01	0.04 ± 0.02	1.79 ± 0.25	0.90 ± 0.01	D
G080.99–50.90	A2552	1208	1.54 ± 0.42	0.27 ± 0.01	0.23 ± 0.03	1.33 ± 0.09	0.65 ± 0.01	10.01 ± 1.13	24.90 ± 3.74	0.75 ± 0.01	M
G083.28–31.03	RXCJ2228.6+2036	1242	1.18 ± 0.03	0.19 ± 0.01	0.22 ± 0.01	2.16 ± 0.09	0.67 ± 0.01	1.40 ± 0.30	2.67 ± 1.01	0.89 ± 0.01	M
G085.99+26.71	A2302	1011	0.24 ± 0.06	0.14 ± 0.01	0.06 ± 0.01	2.83 ± 0.14	0.50 ± 0.01	1.78 ± 0.83	6.76 ± 3.28	0.97 ± 0.01	M
G086.45+15.29		1270	2.23 ± 0.06	0.72 ± 0.01	0.29 ± 0.01	1.02 ± 0.06	0.71 ± 0.01	0.23 ± 0.12	1.05 ± 0.56	0.92 ± 0.01	M
G092.73+73.46	A1763	1271	0.74 ± 0.01	0.17 ± 0.01	0.16 ± 0.01	0.51 ± 0.06	0.66 ± 0.01	4.06 ± 0.52	10.20 ± 1.83	0.79 ± 0.01	M
G093.91+34.90	A2255	1211	0.25 ± 0.01	0.07 ± 0.01	0.08 ± 0.01	1.90 ± 0.06	0.67 ± 0.01	1.35 ± 0.30	0.37 ± 0.30	0.92 ± 0.01	M
G096.87+24.21		1074	0.12 ± 0.01	0.01 ± 0.01	0.04 ± 0.01	6.51 ± 0.22	0.54 ± 0.02	4.10 ± 1.99	2.88 ± 3.42	0.96 ± 0.01	D
G097.73+38.11	A2218	1179	0.73 ± 0.01	0.27 ± 0.01	0.17 ± 0.01	1.38 ± 0.05	0.67 ± 0.01	0.10 ± 0.07	1.00 ± 0.42	0.90 ± 0.01	R
G098.95+24.86	A2312	995	0.92 ± 0.01	0.60 ± 0.01	0.26 ± 0.01	3.15 ± 0.09	0.58 ± 0.01	1.87 ± 0.66	2.67 ± 1.44	0.96 ± 0.01	M
G106.73–83.22	A2813	1132	0.89 ± 0.01	0.11 ± 0.01	0.20 ± 0.01	0.77 ± 0.10	0.72 ± 0.01	0.64 ± 0.28	3.12 ± 1.19	0.95 ± 0.01	R
G107.11+65.31	A1758	1186	0.65 ± 0.01	0.33 ± 0.01	0.11 ± 0.01	1.37 ± 0.05	0.62 ± 0.01	15.30 ± 0.87	12.60 ± 1.56	0.90 ± 0.01	D
G113.82+44.35	A1895	1139	0.46 ± 0.03	0.17 ± 0.01	0.10 ± 0.01	4.65 ± 0.14	0.62 ± 0.01	4.60 ± 1.15	2.00 ± 1.63	0.84 ± 0.01	D
G124.21–36.48	A115N	1072	2.41 ± 0.01	1.00 ± 0.01	0.26 ± 0.01	7.80 ± 0.04	0.66 ± 0.01	74.10 ± 1.40	222.00 ± 5.14	0.65 ± 0.01	D
G125.70+53.85	A1576	1197	1.25 ± 0.20	0.60 ± 0.01	0.20 ± 0.01	1.44 ± 0.15	0.66 ± 0.01	0.09 ± 0.22	1.29 ± 1.81	0.95 ± 0.01	R
G139.19+56.35	A1351	1228	0.51 ± 0.11	0.31 ± 0.01	0.09 ± 0.01	4.60 ± 0.20	0.68 ± 0.01	0.37 ± 0.60	0.71 ± 1.60	0.84 ± 0.01	M
G149.73+34.69	A0665	1353	0.95 ± 0.01	0.56 ± 0.01	0.15 ± 0.01	4.52 ± 0.09	0.71 ± 0.01	0.35 ± 0.25	4.27 ± 1.76	0.95 ± 0.01	M
G157.43+30.33		1125	1.68 ± 0.01	0.98 ± 0.01	0.13 ± 0.01	0.88 ± 0.07	0.61 ± 0.01	0.22 ± 0.23	2.14 ± 1.83	0.93 ± 0.01	M

Table 6
(Continued)

Planck Name	Alternative Name	R_{500} kpc	n_e $\times 10^{-2}$	cusp	c	w $\times 10^{-2}$	Gini	$P30$ $\times 10^{-7}$	$P40$ $\times 10^{-8}$	ell	Dynamical State
G159.85–73.47	A0209	1245	0.81 ± 0.04	0.20 ± 0.01	0.18 ± 0.01	1.02 ± 0.07	0.66 ± 0.01	0.58 ± 0.15	1.26 ± 0.47	0.90 ± 0.01	R
G164.18–38.89	A0399	1119	0.64 ± 0.01	0.46 ± 0.01	0.10 ± 0.01	3.56 ± 0.04	0.66 ± 0.01	1.36 ± 0.18	0.47 ± 0.27	0.85 ± 0.01	M
G166.13+43.39	A0773	1250	0.78 ± 0.01	0.10 ± 0.01	0.22 ± 0.01	1.14 ± 0.06	0.70 ± 0.01	0.01 ± 0.02	0.41 ± 0.24	0.92 ± 0.01	R
G167.65+17.64		1299	0.69 ± 0.01	0.21 ± 0.01	0.16 ± 0.01	0.77 ± 0.07	0.65 ± 0.01	0.03 ± 0.05	0.63 ± 0.40	0.90 ± 0.01	M
G171.94–40.65		1408	0.98 ± 0.01	0.44 ± 0.01	0.17 ± 0.01	1.14 ± 0.07	0.79 ± 0.01	0.09 ± 0.09	0.16 ± 0.25	0.97 ± 0.01	R
G180.24+21.04		1358	1.30 ± 0.04	0.42 ± 0.01	0.12 ± 0.01	1.29 ± 0.05	0.67 ± 0.01	2.09 ± 0.24	3.46 ± 0.60	0.78 ± 0.01	D
G182.44–28.29	A0478	1415	3.00 ± 0.02	0.74 ± 0.01	0.41 ± 0.01	0.10 ± 0.01	0.80 ± 0.01	0.01 ± 0.01	0.11 ± 0.02	0.93 ± 0.01	R
G182.63+55.82	A0963	1126	2.23 ± 0.01	0.60 ± 0.01	0.35 ± 0.01	0.40 ± 0.04	0.73 ± 0.01	0.03 ± 0.03	0.41 ± 0.24	0.97 ± 0.01	R
G186.39+37.25	A0697	1280	0.73 ± 0.01	0.09 ± 0.01	0.16 ± 0.01	0.72 ± 0.20	0.77 ± 0.02	1.39 ± 1.01	0.16 ± 1.07	0.92 ± 0.02	R
G195.62+44.05	A0781	1105	0.34 ± 0.01	0.15 ± 0.01	0.06 ± 0.01	7.11 ± 0.05	0.59 ± 0.01	0.75 ± 0.14	39.50 ± 2.17	0.82 ± 0.01	D
G195.77–24.30	A0520	1314	0.72 ± 0.01	0.76 ± 0.01	0.09 ± 0.01	6.46 ± 0.05	0.63 ± 0.01	0.63 ± 0.15	0.69 ± 0.29	0.98 ± 0.01	D
G218.85+35.50	A0750	1050	0.93 ± 0.01	0.25 ± 0.01	0.25 ± 0.01	4.21 ± 0.09	0.63 ± 0.01	28.20 ± 1.94	54.90 ± 4.61	0.76 ± 0.01	M
G225.92–19.99		1187	3.03 ± 0.02	0.87 ± 0.01	0.21 ± 0.01	8.25 ± 0.12	0.74 ± 0.01	27.90 ± 1.65	31.50 ± 4.45	0.76 ± 0.01	D
G226.17–21.91	A0550	1087	0.57 ± 0.02	0.28 ± 0.01	0.16 ± 0.01	1.64 ± 0.04	0.63 ± 0.01	0.44 ± 0.14	2.99 ± 0.88	0.84 ± 0.01	M
G226.24+76.76	A1413	1215	2.08 ± 0.01	0.74 ± 0.01	0.32 ± 0.01	0.27 ± 0.01	0.79 ± 0.01	0.77 ± 0.02	1.77 ± 0.07	0.80 ± 0.01	M
G228.15+75.19		1239	0.73 ± 0.05	0.10 ± 0.01	0.12 ± 0.01	1.80 ± 0.15	0.59 ± 0.01	0.52 ± 0.39	4.41 ± 1.97	0.95 ± 0.01	D
G228.49+53.12		1061	3.55 ± 0.01	1.05 ± 0.01	0.45 ± 0.01	0.26 ± 0.05	0.77 ± 0.01	0.46 ± 0.16	0.21 ± 0.24	0.89 ± 0.01	R
G229.21–17.24		1136	0.45 ± 0.01	0.23 ± 0.01	0.11 ± 0.01	3.74 ± 0.10	0.54 ± 0.01	2.48 ± 0.56	8.34 ± 2.53	0.79 ± 0.01	M
G229.94+15.29	A0644	1289	1.57 ± 0.01	0.55 ± 0.01	0.34 ± 0.01	2.06 ± 0.01	0.70 ± 0.01	0.32 ± 0.04	0.83 ± 0.13	0.92 ± 0.01	R
G236.95–26.67	A3364	1206	0.77 ± 0.01	0.31 ± 0.01	0.21 ± 0.01	0.87 ± 0.04	0.67 ± 0.01	0.58 ± 0.14	1.09 ± 0.36	0.89 ± 0.01	R
G241.74–30.88	RXCJ0532.9-3701	1159	2.23 ± 0.02	0.63 ± 0.01	0.31 ± 0.01	0.31 ± 0.08	0.73 ± 0.01	0.28 ± 0.18	1.04 ± 0.71	0.92 ± 0.01	R
G241.77–24.00	A3378	1070	3.94 ± 0.01	1.29 ± 0.01	0.41 ± 0.01	0.46 ± 0.02	0.74 ± 0.01	0.04 ± 0.03	0.07 ± 0.10	0.90 ± 0.01	R
G241.97+14.85	A3411	1254	0.46 ± 0.01	0.12 ± 0.01	0.11 ± 0.01	7.11 ± 0.03	0.59 ± 0.01	14.80 ± 0.37	11.50 ± 0.74	0.86 ± 0.01	D
G244.34–32.13	RXCJ0528.9-3927	1229	2.07 ± 0.06	0.67 ± 0.01	0.24 ± 0.01	1.80 ± 0.08	0.74 ± 0.01	0.84 ± 0.19	0.18 ± 0.21	0.97 ± 0.01	M
G244.69+32.49	A0868	1069	0.46 ± 0.01	0.08 ± 0.01	0.15 ± 0.01	2.54 ± 0.15	0.68 ± 0.01	0.25 ± 0.21	2.21 ± 1.42	0.90 ± 0.01	M
G247.17–23.32	ABELLS0579	1031	0.60 ± 0.03	0.25 ± 0.01	0.15 ± 0.10	2.01 ± 0.09	0.57 ± 0.01	1.41 ± 0.47	0.94 ± 0.96	0.87 ± 0.01	M
G249.87–39.86	A3292	948	0.80 ± 0.01	0.20 ± 0.01	0.22 ± 0.01	0.70 ± 0.05	0.63 ± 0.01	1.85 ± 0.65	12.90 ± 3.02	0.90 ± 0.01	R
G250.90–36.25	A3322	1155	0.88 ± 0.01	0.19 ± 0.01	0.23 ± 0.01	1.79 ± 0.06	0.66 ± 0.01	0.28 ± 0.14	1.50 ± 0.73	0.86 ± 0.01	M
G252.96–56.05	A3112	1006	4.08 ± 0.01	1.21 ± 0.01	0.47 ± 0.01	0.52 ± 0.01	0.79 ± 0.01	0.56 ± 0.03	0.99 ± 0.07	0.77 ± 0.01	R
G253.47–33.72	A3343	1118	1.15 ± 0.01	0.60 ± 0.01	0.20 ± 0.01	0.27 ± 0.06	0.69 ± 0.01	0.15 ± 0.13	1.16 ± 0.84	0.96 ± 0.01	R
G256.45–65.71	A3017	1143	1.58 ± 0.02	0.42 ± 0.01	0.26 ± 0.01	1.54 ± 0.05	0.66 ± 0.01	0.34 ± 0.15	3.69 ± 0.92	0.80 ± 0.01	M
G257.34–22.18	A3399	1168	1.11 ± 0.02	0.72 ± 0.01	0.13 ± 0.01	3.14 ± 0.14	0.74 ± 0.01	2.90 ± 0.61	7.36 ± 2.45	0.91 ± 0.01	D
G260.03–63.44	RXCJ0232.2-4420	1196	3.12 ± 0.01	0.79 ± 0.01	0.31 ± 0.01	1.97 ± 0.04	0.75 ± 0.01	0.73 ± 0.17	0.48 ± 0.33	0.97 ± 0.01	R
G262.25–35.36	RXCJ0516.7-5430	1247	0.33 ± 0.01	0.07 ± 0.01	0.07 ± 0.01	6.47 ± 0.13	0.59 ± 0.01	2.09 ± 0.54	0.07 ± 0.24	0.86 ± 0.01	D
G262.71–40.91		1123	1.80 ± 0.02	0.25 ± 0.01	0.30 ± 0.01	1.56 ± 0.06	0.81 ± 0.01	0.40 ± 0.16	0.11 ± 0.15	0.90 ± 0.01	R
G263.16–23.41	AbellS0592	1294	2.71 ± 0.01	0.89 ± 0.01	0.31 ± 0.01	0.50 ± 0.03	0.73 ± 0.01	0.35 ± 0.12	1.69 ± 0.44	0.86 ± 0.01	M
G263.66–22.53	A3404	1297	1.65 ± 0.02	0.56 ± 0.01	0.28 ± 0.01	1.05 ± 0.04	0.71 ± 0.01	0.03 ± 0.03	1.03 ± 0.44	0.86 ± 0.01	M
G266.03–21.25		1499	1.23 ± 0.01	0.44 ± 0.01	0.17 ± 0.01	7.30 ± 0.03	0.74 ± 0.01	0.75 ± 0.09	0.60 ± 0.17	0.92 ± 0.01	D
G269.31–49.87	A3126	1098	0.81 ± 0.01	0.32 ± 0.01	0.25 ± 0.01	0.72 ± 0.05	0.75 ± 0.01	0.27 ± 0.28	4.89 ± 1.97	0.95 ± 0.01	R
G271.19–30.96		1250	4.76 ± 0.08	0.99 ± 0.01	0.38 ± 0.01	0.77 ± 0.05	0.78 ± 0.01	0.11 ± 0.09	0.07 ± 0.14	0.88 ± 0.01	R
G271.50–56.55	S0295	1200	0.90 ± 0.14	0.10 ± 0.01	0.19 ± 0.01	5.80 ± 0.09	0.66 ± 0.01	0.86 ± 0.46	2.60 ± 1.31	0.94 ± 0.01	M
G272.10–40.15	A3266	1316	0.87 ± 0.01	0.61 ± 0.01	0.14 ± 0.01	3.73 ± 0.01	0.61 ± 0.01	0.37 ± 0.03	1.23 ± 0.12	0.86 ± 0.01	D
G277.75–51.73		1238	0.37 ± 0.01	0.04 ± 0.01	0.07 ± 0.01	4.52 ± 0.07	0.58 ± 0.01	2.50 ± 0.38	5.28 ± 0.96	0.86 ± 0.01	D
G278.60+39.17	A1300	1268	2.50 ± 0.01	1.10 ± 0.01	0.20 ± 0.01	3.51 ± 0.08	0.68 ± 0.01	3.90 ± 0.68	0.60 ± 0.69	0.79 ± 0.01	M
G280.19+47.81	A1391	1201	0.51 ± 0.01	0.45 ± 0.01	0.11 ± 0.01	0.47 ± 0.06	0.55 ± 0.01	0.10 ± 0.12	0.32 ± 0.59	0.90 ± 0.01	M
G282.49+65.17	ZwCl1215	1212	0.61 ± 0.02	0.29 ± 0.01	0.16 ± 0.01	0.45 ± 0.02	0.57 ± 0.01	0.60 ± 0.10	1.05 ± 0.26	0.95 ± 0.01	M
G283.16–22.93		1137	1.62 ± 0.01	0.63 ± 0.01	0.19 ± 0.01	1.18 ± 0.11	0.64 ± 0.01	1.98 ± 0.65	1.73 ± 1.60	0.79 ± 0.01	M

Table 6
(Continued)

Planck Name	Alternative Name	R_{500} kpc	n_e $\times 10^{-2}$	cusp	c	w $\times 10^{-2}$	Gini	$P30$ $\times 10^{-7}$	$P40$ $\times 10^{-8}$	ell	Dynamical State
G284.46+52.43	RXJ1206.2-0848	1308	3.39 ± 0.01	0.91 ± 0.01	0.28 ± 0.01	0.67 ± 0.02	0.76 ± 0.01	0.17 ± 0.03	0.37 ± 0.09	0.93 ± 0.01	R
G284.99–23.70		1266	2.56 ± 0.02	0.58 ± 0.01	0.28 ± 0.01	2.42 ± 0.11	0.67 ± 0.01	0.11 ± 0.20	2.37 ± 1.53	0.74 ± 0.01	M
G285.63–17.24		1007	1.76 ± 0.10	1.51 ± 0.01	0.14 ± 0.17	5.25 ± 0.16	0.69 ± 0.01	8.66 ± 2.24	7.55 ± 4.53	0.95 ± 0.01	D
G286.58–31.25		1141	0.61 ± 0.01	0.26 ± 0.01	0.15 ± 0.01	1.03 ± 0.06	0.63 ± 0.01	0.25 ± 0.12	2.33 ± 0.79	0.82 ± 0.01	M
G286.99+32.91		1476	0.66 ± 0.01	0.10 ± 0.01	0.12 ± 0.01	3.82 ± 0.11	0.59 ± 0.01	2.87 ± 0.92	4.82 ± 1.78	0.86 ± 0.01	M
G288.61–37.65	A3186	1301	0.53 ± 0.01	0.16 ± 0.01	0.13 ± 0.01	5.12 ± 0.07	0.63 ± 0.01	1.81 ± 0.37	0.03 ± 0.13	0.91 ± 0.01	M
G292.51+21.98		1147	0.40 ± 0.01	0.22 ± 0.01	0.08 ± 0.01	15.31 ± 0.11	0.59 ± 0.01	227.00 ± 5.21	542.00 ± 19.30	0.67 ± 0.01	D
G294.66–37.02	RXCJ0303.8-7752	1253	0.86 ± 0.01	0.32 ± 0.01	0.17 ± 0.01	2.34 ± 0.09	0.67 ± 0.01	2.50 ± 0.54	6.84 ± 1.86	0.89 ± 0.01	M
G304.67–31.66	A4023	1020	0.43 ± 0.01	0.54 ± 0.01	0.07 ± 0.01	3.07 ± 0.22	0.64 ± 0.02	8.63 ± 2.72	47.10 ± 14.80	0.71 ± 0.01	D
G304.84–41.42		1184	1.47 ± 0.07	0.62 ± 0.01	0.15 ± 0.01	2.40 ± 0.15	0.63 ± 0.01	0.56 ± 0.42	1.97 ± 1.73	0.90 ± 0.01	M
G306.68+61.06	A1650	1102	1.62 ± 0.01	0.71 ± 0.01	0.28 ± 0.01	0.36 ± 0.01	0.71 ± 0.01	0.03 ± 0.01	0.27 ± 0.06	0.89 ± 0.01	R
G306.80+58.60	A1651	1181	1.33 ± 0.01	0.61 ± 0.01	0.27 ± 0.01	0.39 ± 0.03	0.71 ± 0.01	0.14 ± 0.06	0.37 ± 0.20	0.93 ± 0.01	R
G308.32–20.23		1208	1.00 ± 0.01	0.11 ± 0.01	0.17 ± 0.01	0.45 ± 0.07	0.79 ± 0.01	0.27 ± 0.18	0.26 ± 0.42	0.96 ± 0.01	R
G313.36+61.11	A1689	1348	3.08 ± 0.01	0.61 ± 0.01	0.46 ± 0.01	0.63 ± 0.01	0.81 ± 0.01	0.02 ± 0.01	0.01 ± 0.01	0.93 ± 0.01	R
G313.87–17.10		1362	2.22 ± 0.01	0.54 ± 0.01	0.39 ± 0.01	0.47 ± 0.03	0.75 ± 0.01	0.17 ± 0.06	0.69 ± 0.21	0.98 ± 0.01	R
G318.13–29.57		1253	2.18 ± 0.03	0.85 ± 0.01	0.32 ± 0.01	0.60 ± 0.13	0.76 ± 0.02	1.60 ± 0.98	0.02 ± 1.44	0.81 ± 0.02	M
G321.96–47.97	A3921	1082	0.78 ± 0.01	0.40 ± 0.01	0.17 ± 0.01	1.59 ± 0.04	0.63 ± 0.01	8.81 ± 0.29	22.70 ± 1.22	0.72 ± 0.01	M
G324.49–44.97	RXCJ2218.0-6511	974	1.33 ± 0.01	0.86 ± 0.01	0.20 ± 0.01	0.61 ± 0.06	0.60 ± 0.01	0.39 ± 0.19	0.34 ± 0.39	0.86 ± 0.01	R
G332.23–46.36	A3827	1236	0.98 ± 0.01	0.38 ± 0.01	0.23 ± 0.01	0.58 ± 0.03	0.67 ± 0.01	0.36 ± 0.06	0.64 ± 0.18	0.94 ± 0.01	R
G332.88–19.28		1209	1.18 ± 0.21	0.65 ± 0.01	0.22 ± 0.01	1.09 ± 0.05	0.72 ± 0.01	0.75 ± 0.36	1.19 ± 1.01	0.95 ± 0.01	M
G335.59–46.46	A3822	1244	0.43 ± 0.01	0.21 ± 0.01	0.11 ± 0.01	0.94 ± 0.04	0.60 ± 0.01	0.59 ± 0.20	5.11 ± 0.91	0.94 ± 0.01	M
G336.59–55.44	A3911	1086	0.34 ± 0.01	0.29 ± 0.01	0.09 ± 0.01	1.63 ± 0.04	0.58 ± 0.01	0.04 ± 0.03	1.21 ± 0.27	0.86 ± 0.01	M
G337.09–25.97		922	2.40 ± 0.15	0.94 ± 0.01	0.40 ± 0.01	1.09 ± 0.07	0.60 ± 0.01	15.40 ± 1.33	61.50 ± 6.27	0.80 ± 0.01	M
G342.31–34.90		1572	0.64 ± 0.05	0.22 ± 0.01	0.16 ± 0.01	0.51 ± 0.15	0.74 ± 0.02	1.16 ± 0.76	0.73 ± 1.66	0.90 ± 0.02	M
G347.18–27.35	S0821	1246	0.67 ± 0.01	0.37 ± 0.01	0.08 ± 0.01	2.52 ± 0.09	0.57 ± 0.01	0.50 ± 0.20	1.17 ± 0.77	0.96 ± 0.01	M
G349.46–59.94	AS1063	1446	2.91 ± 0.04	0.62 ± 0.01	0.33 ± 0.01	0.88 ± 0.02	0.79 ± 0.01	0.03 ± 0.01	0.90 ± 0.17	0.87 ± 0.01	R

Note. The last column indicates whether the cluster was visually classified as relaxed (R), mix (M), or disturbed (D).

Appendix I
Parameter-parameter Correlations

In Table 7 we list all the correlation coefficients and relative p-values for the plots shown in Figure 2.

Table 7
Pearson and Spearman Rank Test Correlation and Probability for no Correlation between Pairs of Morphological Parameters Computed within R_{500}

	R_{500}			
Relation	ρ	p-value	r	p-value
n_e–c	0.87	<0.01	0.87	<0.01
n_e–Gini	0.66	<0.01	0.73	<0.01
n_e–w	−0.29	<0.01	−0.42	<0.01
n_e–P30	−0.06	0.48	−0.34	<0.01
n_e–$P40$	−0.06	0.50	−0.33	<0.01
n_e–α	0.79	<0.01	0.81	<0.01
n_e–ell	0.02	0.85	0.05	0.60
c − Gini	0.71	<0.01	0.71	<0.01
c − w	−0.44	<0.01	−0.53	<0.01
c–P30	−0.11	0.24	−0.39	<0.01
c–$P40$	−0.10	0.30	−0.37	<0.01
c–α	0.64	<0.01	0.60	<0.01
c − ell	0.08	0.41	0.08	0.39
Gini − w	−0.35	<0.01	−0.40	<0.01
Gini–P30	−0.14	0.13	−0.37	<0.01
Gini–$P40$	−0.14	0.12	−0.49	<0.01
Gini–α	0.46	<0.01	0.46	<0.01
Gini − ell	0.18	0.05	0.20	0.03
w–P30	0.63	<0.01	0.53	<0.01
w–$P40$	0.61	<0.01	0.45	<0.01
w–α	−0.22	0.02	−0.32	<0.01
w − ell	0.18	0.05	0.20	0.03
P30–$P40$	0.99	<0.01	0.56	<0.01
P30–α	−0.04	0.68	−0.27	<0.01
P30–ell	−0.43	<0.01	−0.40	<0.01
$P40$–α	−0.03	0.77	−0.26	<0.01
$P40$–ell	−0.44	<0.01	−0.38	<0.01
α–ell	−0.03	0.71	−0.03	0.74

ORCID iDs

William R. Forman https://orcid.org/0000-0002-9478-1682
Felipe Andrade-Santos https://orcid.org/0000-0002-8144-9285
Scott Randall https://orcid.org/0000-0002-3984-4337
Ralph Kraft https://orcid.org/0000-0002-0765-0511

References

Abraham, R. G., van den Bergh, S., & Nair, P. 2003, ApJ, 588, 218
Andrade-Santos, F., Jones, C., Forman, W. R., et al. 2017, ApJ, 843, 76
Andrade-Santos, F., Lima Neto, G. B., & Laganá, T. F. 2012, ApJ, 746, 139
Angulo, R. E., Springel, V., White, S. D. M., et al. 2012, MNRAS, 426, 2046
Applegate, D. E., Mantz, A., Allen, S. W., et al. 2016, MNRAS, 457, 1522
Arnaud, K. A. 1996, in ASP Conf. Ser. 101, Astronomical Data Analysis Software and Systems V, ed. G. H. Jacoby & J. Barnes (San Francisco, CA: ASP), 17
Arnaud, M., Pointecouteau, E., & Pratt, G. W. 2005, A&A, 441, 893
Arnaud, M., Pratt, G. W., Piffaretti, R., et al. 2010, A&A, 517, A92
Bartalucci, I., Arnaud, M., Pratt, G. W., et al. 2017, A&A, 598, A61
Böhringer, H., Pratt, G. W., Arnaud, M., et al. 2010, A&A, 514, A32
Borm, K., Reiprich, T. H., Mohammed, I., & Lovisari, L. 2014, A&A, 567, A65
Buote, D. A., & Tsai, J. C. 1995, ApJ, 452, 522
Buote, D. A., & Tsai, J. C. 1996, ApJ, 458, 27
Burenin, R. A., Vikhlinin, A., Hornstrup, A., et al. 2007, ApJS, 172, 561
Cassano, R., Ettori, S., Giacintucci, S., et al. 2010, ApJL, 721, L82
Cuciti, V., Cassano, R., Brunetti, G., et al. 2015, A&A, 580, A97
Donahue, M., Ettori, S., Rasia, E., et al. 2016, ApJ, 819, 36
Eckert, D., Ettori, S., Pointecouteau, E., et al. 2017, AN, 338, 293
Eckert, D., Molendi, S., & Paltani, S. 2011, A&A, 526, A79
Fakhouri, O., Ma, C.-P., & Boylan-Kolchin, M. 2010, MNRAS, 406, 2267
Hudson, D. S., Mittal, R., Reiprich, T. H., et al. 2010, A&A, 513, A37
Israel, H., Reiprich, T. H., Erben, T., et al. 2014, A&A, 564, A129
Jones, C., & Forman, W. 1984, ApJ, 276, 38
Jones, C., & Forman, W. 1999, ApJ, 511, 65
Lau, E. T., Kravtsov, A. V., & Nagai, D. 2009, ApJ, 705, 1129
Lin, H. W., McDonald, M., Benson, B., & Miller, E. 2015, ApJ, 802, 34
Lotz, J. M., Primack, J., & Madau, P. 2004, AJ, 128, 163
Lovisari, L., Reiprich, T. H., & Schellenberger, G. 2015, A&A, 573, A118
Lovisari, L., Schindler, S., & Kapferer, W. 2011, A&A, 528, A60
Mann, A. W., & Ebeling, H. 2012, MNRAS, 420, 2120
Mantz, A. B., Allen, S. W., Morris, R. G., et al. 2015, MNRAS, 449, 199
McDonald, M., Allen, S. W., Bayliss, M., et al. 2017, arXiv:1702.05094
Mohr, J. J., Fabricant, D. G., & Geller, M. J. 1993, ApJ, 413, 492
Motl, P. M., Hallman, E. J., Burns, J. O., & Norman, M. L. 2005, ApJL, 623, L63
Nurgaliev, D., McDonald, M., Benson, B. A., et al. 2013, ApJ, 779, 112
Nurgaliev, D., McDonald, M., Benson, B. A., et al. 2017, ApJ, 841, 5
Parekh, V., van der Heyden, K., Ferrari, C., Angus, G., & Holwerda, B. 2015, A&A, 575, A127
Pinkney, J., Roettiger, K., Burns, J. O., & Bird, C. M. 1996, ApJS, 104, 1
Planck Collaboration, Ade, P. A. R., Aghanim, N., et al. 2011b, A&A, 536 A8
Planck Collaboration, Ade, P. A. R., Aghanim, N., et al. 2013, A&A, 550, A130
Planck Collaboration, Ade, P. A. R., Aghanim, N., et al. 2014, A&A, 571 A20
Planck Collaboration, Aghanim, N., Arnaud, M., et al. 2011a, A&A, 536, A9
Pratt, G. W., Croston, J. H., Arnaud, M., & Böhringer, H. 2009, A&A, 498, 361
Randall, S. W., Sarazin, C. L., & Ricker, P. M. 2002, ApJ, 577, 579
Rasia, E., Ettori, S., Moscardini, L., et al. 2006, MNRAS, 369, 2013
Rasia, E., Meneghetti, M., & Ettori, S. 2013, AstRv, 8, 40
Reiprich, T. H., & Böhringer, H. 2002, ApJ, 567, 716
Ricker, P. M., & Sarazin, C. L. 2001, ApJ, 561, 621
Roncarelli, M., Ettori, S., Dolag, K., et al. 2006, MNRAS, 373, 1339
Rossetti, M., Gastaldello, F., Eckert, D., et al. 2017, MNRAS, 468, 1917
Rossetti, M., Gastaldello, F., Ferioli, G., et al. 2016, MNRAS, 457, 4515
Santos, J. S., Rosati, P., Tozzi, P., et al. 2008, A&A, 483, 35
Smith, R. K., Brickhouse, N. S., Liedahl, D. A., & Raymond, J. C. 2001, ApJL, 556, L91
Sunyaev, R. A., & Zeldovich, Y. B. 1972, CoASP, 4, 173
Tchernin, C., Eckert, D., Ettori, S., et al. 2016, A&A, 595, A42
Ventimiglia, D. A., Voit, G. M., Donahue, M., & Ameglio, S. 2008, ApJ, 685, 118
Vikhlinin, A., Burenin, R., Forman, W. R., et al. 2007, in Heating Versus Cooling in Galaxies and Clusters of Galaxies, ed. H. Böhringer et al. (Berlin: Springer), 48
Weißmann, A., Böhringer, H., Šuhada, R., & Ameglio, S. 2013, A&A, 549, A19
Willingale, R., Starling, R. L. C., Beardmore, A. P., Tanvir, N. R., & O'Brien, P. T. 2013, MNRAS, 431, 394
Zhang, Y.-Y., Reiprich, T. H., Finoguenov, A., Hudson, D. S., & Sarazin, C. L. 2009, ApJ, 699, 1178